Научном већу
Института за физику
Прегревица 118, Земун

Предмет: Реизбор у звање истраживач сарадник

Молим Научно веће Института за физику да покрене поступак за мој реизбор у звање истраживач сарадник.

Прилажем:

• Мишљење руководиоца пројекта
• Биографију
• Списак научних радова
• Фотокопије научних радова
•Потврду о упису на докторске академске студије
•Потврду о завршеним основним академскими дипломским академским студијама
•Преглед научне активности

С поштовањем,

Душан Грујић

Мишљење руководиоца пројекта

Молим Научно веће Института за физику

да покрене поступак за реизбор Душана Грујића у звање истраживач сарадник. Колега Грујић је уписан на Докторске академске студије на Физичком факултету, Универзитета у Београду, смер Квантна оптика и ласери. Учествовао је у изради пет радова у међународним часописима. Колега Грујић ангажован је на пројекту ИИИ 45016 Министарства просвете, науке и технолошког развоја "Генерисање и карактеризација нанофотонских функционалних структура у биомедицини". Резултати које је постигао колега Грујић показују да поседује неопходне способности за израду докторске дисертације, као и да се активно бави научно-истраживачким радом. Овим наведеним, колега задовољава све неопходне услове Министарства просвете, науке и технолошког развој за реизбор у звање истраживач сарадник. За чланове Комисије у поступку реизбора предлажем:

- др Бранислава Јеленковића - научни саветник, Институт за физику у Београду
- др Дејана Пантелића - научни саветник, Институт за физику у Београду
- др Зорана Николића - доцент, Физички факултету у Београду

Уз поштовање,

Руководилац пројекта ИИИ 45016 Министарства просвете, науке и технолошког развоја

Научни саветник Института за физику,

др Бранислав Јеленковић

Биографија кандидата

Душан Грујић је рођен у Крушевцу, Република Србија, 24.02.1984. године. У Крушевцу је завршио основну школу и Гимназију, природно – математички смер. 2010. године дипломира (основне академске студије) на Физичком факултету, Универзитета у Београду, смер Примењена физика и информатика са просечном оценом 8,14. Дипломски рад је одбранио на тему „Примена нумеричких метода у анализама Cole-Cole дијаграма“. Од 01.01. 2011. године је запослен у Институту за физику, са ангажовањем на пројекту Министарства просвете, науке и технолошког развоја "Генерисање и карактеризација нанофотонских функционалних структура у биомедицини и информатици". Од јануара 2012. године је уписан на Докторске академске студије Физичког факултета Универзитета у Београду, смер Квантна оптика и ласери и тренутно је на трећој години. До сада је публиковао два научна рада у часопису категорије М21, три научна рада у часопису категорије М22 и један категорије М60.

Списак објављених радова

(1) N. M. Lučić, D. M. Jović Savić, A. Piper, D. Ž. Grujić, J. M. Vasiljević, D. V. Pantelić, B. M. Jelenković, and D. V. Timotijević, *Light propagation in quasiperiodic Fibonacci waveguide arrays*, J. Opt. Soc. Am. B32 7 1510 (2015)–**M22** (doi: 10.1364/JOSAB.32.001510, IF = 1.970)

(2) Dejan V. Pantelić, Dušan Ž. Grujić, Darko M. Vasiljević, *Single-beam, dual-view digital holographic interferometry for biomechanical strain measurements of biological objects* , J. Biomed. Opt. 19(12), 127005 (2014) – **M21** (doi:10.1117/1.JBO.19.12.127005, IF = 2.926)

(3) D Pantelić, S Savić-Šević and D Grujić, *Zoom system for measurement of coherent backscattering of light in micro- and nanomaterials*, Physica Scripta T 157 014020 (2013) – **M22** (doi: 10.1088/0031-8949/2013/T157/014020, IF=1.103)

(4) N. M. Lučić, B. M. Bokić, D. Ž. Grujić, D. V. Pantelić, B. M. Jelenković, A. Piper, D. M. Jović, and D. V. Timotijević, *Defect-guided Airy beams in optically induced waveguide arrays*, Phys. Rev. A 88, 063815 (2013)– **M21** (doi: 10.1103/PhysRevA.88.063815, IF = 3.042)

(5) Boban Zarkov, Dušan Grujić and Dejan Pantelić, *High-resolution dot-matrix hologram generation*, Physica Scripta T 149 014021 (2012) – **M22** (doi: 10.1088/0031-8949/2012/T149/014021, IF=1.103)

(6) Dejan Pantelić, Dušan Grujić, Darko Vasiljević, *Praktične primene digitalne holografije*, Zbornik apstrakata Šesta radionica fotonike 2013 (ISBN 978-86-82441-35-9) – **M60**

Journal of the Optical Society of America B
OPTICAL PHYSICS

Light propagation in quasi-periodic Fibonacci waveguide arrays

N. M. Lučić, D. M. Jović Savić,* A. Piper, D. Ž. Grujić, J. M. Vasiljević, D. V. Pantelić, B. M. Jelenković, and D. V. Timotijević

Institute of Physics, University of Belgrade, P.O. Box 68, 11001 Belgrade, Serbia
**Corresponding author: jovic@ipb.ac.rs*

Received 26 March 2015; revised 19 May 2015; accepted 3 June 2015; posted 5 June 2015 (Doc. ID 236998); published 26 June 2015

We investigate light propagation along one-dimensional quasi-periodic Fibonacci waveguide array optically induced in Fe:$LiNbO_3$ crystal. Two Fibonacci elements, A and B, are used as a separation between waveguides. We demonstrate numerically and experimentally that a beam expansion in such arrays is effectively reduced compared to the periodic ones, without changing beam expansion scaling law. The influence of refractive index variation on the beam expansion in such systems is discussed: more pronounced diffraction suppression is observed for a higher refractive index variation.

OCIS codes: (050.5298) Photonic crystals; (190.5330) Photorefractive optics.

http://dx.doi.org/10.1364/JOSAB.32.001510

1. INTRODUCTION

The discovery of quasi-crystals in condensed matter by Shechtman *et al.* [1] and their theoretical analysis by Levine and Steinhardt [2] has inspired a new field of research in optics and photonics.

Examples in the field of optics are photonic quasi-crystals with dielectric multilayers forming the Fibonacci sequence as proposed by Kohmoto *et al.* [3], and realized in [4–6], as well as other deterministic aperiodic structures with long-range order [7,8]. Photonic quasi-crystals have peculiar optical properties. Namely, they lie between periodic and disordered structures and exhibit unique and rich symmetries in Fourier space that are not possible within periodic lattices. The large variety of aperiodic structures is very important and could provide significant flexibility and richness when engineering the optical response of devices [9].

The localization of waves is a ubiquitous phenomenon observed in a variety of classical and quantum systems [10–12], including light waves [13–16], Bose–Einstein condensates [17,18], and sound waves [19]. Although stated more than 50 years ago [11], Anderson localization is still one of the most appealing approaches in optical wave manipulation. In this regard, a transverse localization of light in waveguide lattices turns out to be a particularly interesting concept [13,14]. As the transverse expansion properties in periodic photonic lattices [20–23], as well as in disordered ones [14,24–26], have been investigated extensively, the quasi-periodic photonic lattices emerged as a further attractive research field. The light localization in the Aubry–André model of a quasi-periodic lattice is observed [27], but the transverse expansion in many other models of photonic quasi-crystals [28] is still an open question.

In this paper, we extend these concepts to the beam expansion in quasi-periodic Fibonacci waveguide arrays, considering light propagation along waveguides. We fabricate the array of identical waveguides (identical refractive index profile). The distance between successive waveguides is modulated in the Fibonacci manner. This means that the sequence of separations consists of two elements, A and B, lined in such a way to make a Fibonacci word. We consider how various input beam positions (incident positions) influence diffraction, and compare them with appropriate periodic waveguide arrays. In general, we find the beam expansion is slowed in quasi-periodic Fibonacci waveguide arrays. Increasing the refractive index variation, the effect is more pronounced.

2. EXPERIMENTAL SETUP AND THEORETICAL BACKGROUND

For the experimental realization of the Fibonacci waveguide array we use $LiNbO_3$ crystal, doped with 0.05% of iron. Dimensions of the crystal are 3 mm × 0.5 mm × 10 mm, with the optical axis along the z direction (10 mm). Waveguides are fabricated using an in-house developed laser writing system with a CW laser at 473 nm and a precise two-axis positioning platform. The platform can move the crystal in the x–z plane. The laser beam propagates along the y axis and it is focused by the 50× microscope objective slightly below the upper surface of the crystal. In this way, the laser makes a controllable local change of the refractive index. By moving the sample along the

z direction, a uniform modification of the refractive index profile is achieved [Fig. 1(a)]. The width of the waveguide obtained in this way is approximately 5 μm with a maximum refractive index variation of $\Delta n \sim 1 \times 10^{-4}$, estimated from numerical simulations. The distances between the centers of the adjacent waveguides are $a = 10$ μm and $b = 16.18$ μm, and follow the Fibonacci word rule, with the golden ratio $b/a = (1 + \sqrt{5})/2$ in our case [Fig. 1(c)].

A scheme of the experimental setup is shown in Fig. 1(b). A beam from He:Ne laser, after appropriate preparation, is focused on the front face of the crystal and propagates along the z direction. The beam waist is around 10.5 μm and the power is 10 nW. The light is polarized linearly in the y direction. The crystal is situated in a holder which can be moved in the x direction in small steps. In this way, we can launch the beam into appropriate position in the waveguide array. The intensity pattern appearing at the exit face of the crystal is observed by means of an imaging system which consists of a microscope objective and CCD camera.

To theoretically model light propagation in quasi-periodic Fibonacci waveguide arrays, along the propagation distance z, we consider the paraxial wave equation for the slowly varying electric field amplitude E:

$$i\frac{\partial E}{\partial z} = -\frac{1}{2}\frac{\partial^2 E}{\partial x^2} - V(x)E, \tag{1}$$

where $V(x) = n_s + \Delta n \sum_{i=1}^{N} e^{-(x-x_i)^2/2\sigma^2}$ is the quasi-periodic refractive index profile of the array, n_s is a bulk material refractive index, and Δn is an optically induced refractive index variation. The two Fibonacci elements, A and B, are used as a separation between the waveguides a and b [see Fig. 1(c)]. An array of N waveguides modeled with Gaussian functions centered at x_i is spaced to follow some Fibonacci word. For example, we experimentally realized a waveguide array that represents the following Fibonacci word: ABAABABAABAABABAABA (the first 20 elements) [see Fig. 1(c)]. For solving our model equation, we use the split-step method with the parameters of our experiment.

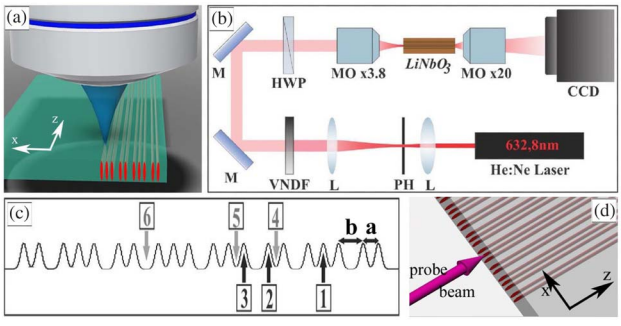

Fig. 1. Setup for an investigation of light propagation in Fibonacci waveguide arrays. (a) Scheme of the laser writing waveguide arrays process in an Fe:$LiNbO_3$ crystal. (b) Schematic of the experimental setup: He:Ne laser at 632.8 nm; L, lens; PH, pinhole; VNDF, variable neutral density filter; M, mirror; HWP, half-wave plate; MO, microscope objective; CCD, camera. (c) A schematic of a refractive index profile used in numerics ($V(x)$), with two separations between waveguides, a and b. Arrows with numbers show incident beam positions inside waveguides (black) and between waveguides (gray). (d) Schematic geometry of Fibonacci lattice with Gaussian probe beam.

3. LIGHT PROPAGATION IN FIBONACCI WAVEGUIDE ARRAYS: EXPERIMENT VERSUS THEORY

We consider beam propagating in Fibonacci waveguide arrays fabricated in our crystal, launched at different incident positions. The propagation characteristics are obtained numerically and experimentally; Fig. 2 summarizes our results. We choose three typical incident positions *inside* waveguides marked by numbers 1, 2, and 3 in Fig. 1(c). Propagations from these positions are represented in the first, second, and third row in Fig. 2. The first column presents intensity distribution along the propagation distance observed numerically, with output profiles in the second column. Experimental results for the same incident positions are presented as intensity distributions at the exit face of the crystal (the forth column) with corresponding profiles in the third column. One can see a very good agreement with numerically obtained profiles.

The main reason for more pronounced diffraction suppression for incident beam positions 1 and 2 [Figs. 2(b) and 2(f)], in comparison with position 3 [Fig. 2(j)], is the separation between incident and neighboring waveguides. While propagating in the medium, the beam displays slowing of beam expansion, compared to the appropriate periodic waveguide arrays [Fig. 4(b)].

Next, we study beam propagating characteristics for incident positions *between* waveguides marked by numbers 4, 5, and 6 in Fig. 1(c). Figure 3 summarizes our numerical and experimental results for these cases. The layout of this figure is the same as in Fig. 2: incident positions 4, 5, and 6 in Fig. 1(c) correspond to the results in the first, second, and third row in Fig. 3, respectively. Beam diffraction for incident positions

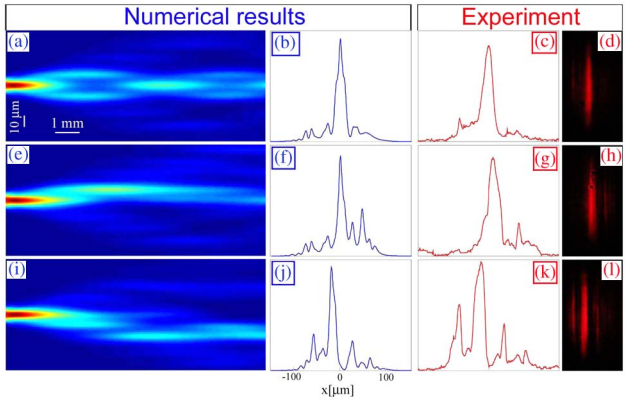

Fig. 2. Light propagation in Fibonacci waveguide arrays. Incident positions of the beam are *inside* certain waveguides, marked with numbers in Fig. 1(c): the first row corresponds to the position 1; the second row corresponds to 2; and the third row corresponds to 3. Intensity distributions of the beam in longitudinal direction during the propagation: (a), (e), and (i) observed numerically. Corresponding intensity profiles at the exit face of the crystal observed numerically: (b), (f), and (j) and experimentally (c), (g), and (k). Experimentally measured intensity distributions at the exit face of the crystal (d), (h), and (l). Physical parameters: the crystal length $L = 1$ cm, refractive index variation $\Delta n = 1 \times 10^{-4}$, and Gaussian beam width 10 μm.

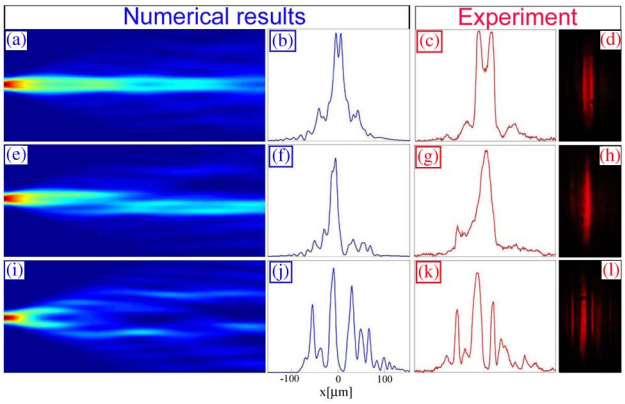

Fig. 3. Light propagation in Fibonacci waveguide arrays with incident positions of the beam *between* certain waveguides, marked with numbers in Fig. 1(c): position 4 corresponds to the first row, 5 to the second row, and 6 to the third row. Intensity distributions of the beam in longitudinal direction during the propagation: (a), (e), and (i) observed numerically. Corresponding intensity profiles at the exit face of the crystal observed numerically (b), (f), and (j) and experimentally (c), (g), and (k). Experimentally measured intensity distributions at the exit face of the crystal (d), (h), and (l). Physical parameters are as in Fig. 2.

between waveguides is more pronounced than for incident positions *inside* waveguides (Fig. 2), but again less pronounced then in periodic waveguide arrays [Fig. 4(b)]. One can see a more pronounced tendency toward diffraction suppression for incident beam position 5 [Fig. 3(g)], compared with 4 [Fig. 3(c)] and 6 [Fig. 3(k)]. We want to stress that these conclusions are relevant only for the distance of propagation in our experiment (1 cm). More general conclusions are drawn in the next chapter, where numerical simulations are performed on longer propagation distances.

4. LIGHT PROPAGATION IN WAVEGUIDE ARRAYS: PERIODIC VERSUS FIBONACCI

We study numerically the beam propagation in Fibonacci waveguide arrays considering longer propagation distances ($L = 10$ cm). To characterize the level of beam expansion, we use the effective beam width $\omega_{\text{eff}} = P^{-1/2}$, where $P = \int |E|^4(x, L)\mathrm{d}x / \{\int |E|^2(x, L)\mathrm{d}x\}^2$ is the inverse participation ratio. In such a system, it is useful to perform averaging over different incident beam positions to remove the effects of the local environment, i.e., the influence of the neighboring waveguides. Averaged effective beam width is calculated along the propagation distance, and compared for the Fibonacci waveguide array and three different periodic waveguide arrays. Separations a and b in Fibonacci waveguide arrays are used as periods $d = 16.18$ μm and $d = 10$ μm for two periodic waveguide arrays. The third periodic array is produced in such a way that the same number of waveguides as in quasi-periodic is arranged in periodic manner in the same space (in our geometry, its lattice period is $d = 12.38$ μm), aimed as the most appropriate for comparison with Fibonacci waveguide array.

Figure 4(a) presents the averaged effective width (averaged over incident positions) along the propagation distance for Fibonacci lattice and refractive index variation $\Delta n = 1 \times 10^{-4}$,

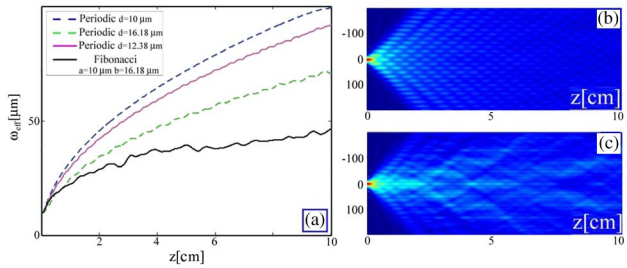

Fig. 4. Comparison between beam diffraction in periodic and quasi-periodic waveguide arrays. (a) Averaged effective beam widths versus the propagation distance, for refractive index variation $\Delta n = 1 \times 10^{-4}$. (b) Field intensity of the beam in longitudinal direction (z) during the propagation for periodic lattice with $d = 12.38$ μm. (c) Averaged field intensity distribution for Fibonacci lattice. Crystal length is $L = 10$ cm.

with the effective beam width for all previously mentioned periodic lattices for the same value of refractive index variation. It should be stressed that the beam width increases more slowly in a Fibonacci lattice compared to the periodic lattices. Clearly, the beam propagation in periodic lattice with $d = 10$ μm displays the strongest discrete diffraction, followed by other periodic lattices and then quasi-periodic. We also observe that the Fibonacci lattice follows the same beam expansion scaling law [29]. For shorter propagation distances (up to 1.5 cm), beam diffraction in the periodic lattice with $d = 16.18$ μm is slightly less pronounced than in quasi-periodic because of the weaker coupling between adjacent waveguides in that lattice.

Figure 4(b) presents a typical beam spreading along the propagation distance, for a periodic lattice with $d = 12.38$ μm, simulated for 10 cm of propagation. The averaged intensity distribution for hundreds of different incident positions in a Fibonacci lattice is presented in Fig. 4(c). Compared with the appropriate periodic lattice [Fig. 4(b)], a tendency of Fibonacci lattice to suppress diffraction is evident [Fig. 4(c)].

5. DEPENDENCE OF LIGHT PROPAGATION ON THE REFRACTIVE INDEX VARIATION

At the end, we study the influence of various refractive index variations (Δn) on the beam propagation in Fibonacci waveguide arrays. Again, we calculate the averaged effective width along the propagation distance for each value of Δn. The increase of refractive index variation makes diffraction suppression more pronounced [Fig. 5(a)]: the broadening of the beam becomes almost completely suppressed for longer propagation distances. These curves show a transition from ballistic spreading (normal diffusion) to anomalous diffusion. In addition, a higher refractive index variation changes the anomalous diffusion behavior. The averaged intensity distribution, for hundreds of different incident positions, is presented for $\Delta n = 2 \times 10^{-4}$ in Fig. 5(b), and $\Delta n = 4 \times 10^{-4}$ in Fig. 5(c). These should be compared with the corresponding distribution in Fig. 4(c) for $\Delta n = 1 \times 10^{-4}$. The tendency to suppress diffraction is evident as for a higher refractive index variation; a larger portion of the beam is confined between adjacent waveguides.

Typical averaged intensity distribution profiles in longitudinal direction for propagation lengths of 2, 3, and 4 cm are presented

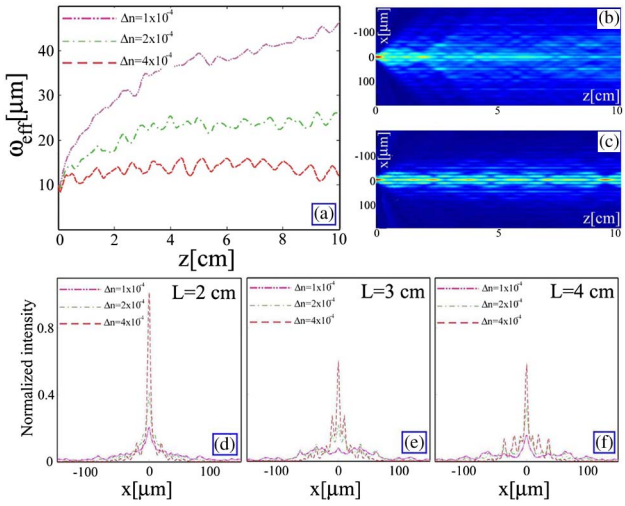

Fig. 5. Light propagation in Fibonacci lattice for a higher refractive index variation. (a) Comparison between propagation in waveguide arrays with different refractive index variation: averaged effective beam widths versus the propagation distance. Averaged field intensity distributions for (b) $\Delta n = 2 \times 10^{-4}$ and (c) $\Delta n = 4 \times 10^{-4}$. Intensity distribution profiles for the same values of Δn at different propagation distances: (d) 2 cm, (e) 3 cm, and (f) 4 cm.

for three values of refractive index variation: $\Delta n = 1 \times 10^{-4}$, $\Delta n = 2 \times 10^{-4}$, and $\Delta n = 4 \times 10^{-4}$ [Figs. 5(d)–5(f)]. Again, one can see a transition toward stronger diffraction suppression with a higher refractive index variation.

6. CONCLUSIONS

In summary, we have observed the beam expansion is slowed down in optically induced Fibonacci waveguide arrays. We have analyzed experimentally and numerically how various incident positions influence propagation characteristics. The experimental results fully agree with the theoretical analysis. Diffraction suppression is observed with Fibonacci waveguide arrays, compared to the appropriate periodic waveguide arrays. We have investigated the influence of refractive index variation on the beam spreading in Fibonacci waveguide arrays. More pronounced diffraction suppression is observed for higher refractive index variations.

Funding. Ministry of Education, Science and Technological Development, Republic of Serbia (OI 171036, OI 171038, III 45016).

REFERENCES

1. D. Shechtman, I. Blech, D. Gratias, and J. W. Cahn, "Metallic phase with long-range orientational order and no translational symmetry," Phys. Rev. Lett. **53**, 1951–1953 (1984).
2. D. Levine and P. J. Steinhardt, "Quasicrystals: a new class of ordered structures," Phys. Rev. Lett. **53**, 2477–2480 (1984).
3. M. Kohmoto, B. Sutherland, and K. Iguchi, "Localization in optics: quasiperiodic media," Phys. Rev. Lett. **58**, 2436–2438 (1987).
4. G. Gumbs and M. K. Ali, "Dynamical maps, Cantor spectra, and localization for Fibonacci and related quasiperiodic lattices," Phys. Rev. Lett. **60**, 1081–1084 (1988).
5. W. Gellermann, M. Kohmoto, B. Sutherland, and P. C. Taylor, "Localization of light waves in Fibonacci dielectric multilayers," Phys. Rev. Lett. **72**, 633–636 (1994).
6. L. D. Negro, C. J. Oton, Z. Gaburro, L. Pavesi, P. Johnson, A. Lagendijk, R. Righini, M. Colocci, and D. S. Wiersma, "Light transport through the band-edge states of Fibonacci quasicrystals," Phys. Rev. Lett. **90**, 055501 (2003).
7. W. Steurer and D. Sutter-Widmer, "Photonic and phononic quasicrystals," J. Phys. D **40**, R229–R247 (2007).
8. E. L. Albuquerque and M. G. Cottam, "Theory of elementary excitations in quasiperiodic structures," Phys. Rep. **376**, 225–337 (2003).
9. Z. V. Vardeny, A. Nahata, and A. Agrawal, "Optics of photonic quasicrystals," Nat. Photonics **7**, 177–187 (2013).
10. P. Sheng, *Scattering and Localization of Classical Waves in Random Media* (World Scientific, 1990).
11. A. Lagendijk, B. Tiggelen, and D. S. Wiersma, "Fifty years of Anderson localization," Phys. Today **62**(8), 24–29 (2009).
12. S. S. Abdullaev and F. Kh. Abdullaev, "On the light propagation in the system of tunnel-coupled waveguides," Sov. J. Radiofizika **23**, 766 (1980).
13. T. Pertsch, U. Peschel, J. Kobelke, K. Schuster, H. Bartelt, S. Nolte, A. Tünnermann, and F. Lederer, "Nonlinearity and disorder in fiber arrays," Phys. Rev. Lett. **93**, 053901 (2004).
14. T. Schwartz, G. Bartal, S. Fishman, and M. Segev, "Transport and Anderson localization in disordered two-dimensional photonic lattices," Nature **446**, 52–55 (2007).
15. S. Gentilini, A. Fratalocchi, L. Angelani, G. Ruocco, and C. Conti, "Ultrashort pulse propagation and the Anderson localization," Opt. Lett. **34**, 130 (2009).
16. C. Conti and A. Fratalocchi, "Dynamic light diffusion, three-dimensional Anderson localization and lasing in inverted opals," Nat. Phys. **4**, 794–798 (2008).
17. G. Roati, C. D'Errico, L. Fallani, M. Fattori, C. Fort, M. Zaccanti, G. Modugno, M. Modugno, and M. Inguscio, "Anderson localization of a non-interacting Bose–Einstein condensate," Nature **453**, 895–898 (2008).
18. J. Billy, V. Josse, Z. Zuo, A. Bernard, B. Hambrecht, P. Lugan, D. Clément, L. Sanchez-Palencia, P. Bouyer, and A. Aspect, "Direct observation of Anderson localization of matter waves in a controlled disorder," Nature **453**, 891–894 (2008).
19. J. D. Maynard, "Acoustical analogs of condensed-matter problems," Rev. Mod. Phys. **73**, 401–417, (2001).
20. H. S. Eisenberg, Y. Silberberg, R. Morandotti, and J. S. Aitchison, "Diffraction management," Phys. Rev. Lett. **85**, 1863–1866 (2000).
21. T. Pertsch, T. Zentgraf, U. Peschel, A. Bräuer, and F. Lederer, "Anomalous refraction and diffraction in discrete optical systems," Phys. Rev. Lett. **88**, 093901 (2002).
22. D. N. Christodoulides, F. Lederer, and Y. Silberberg, "Discretizing light behavior in linear and nonlinear waveguide lattices," Nature **424**, 817–823 (2003).
23. A. Fratalocchi and G. Assanto, "Light propagation through a nonlinear defect: symmetry breaking and controlled soliton emission," Opt. Lett. **31**, 1489–1491 (2006).
24. D. M. Jović, Yu. S. Kivshar, C. Denz, and M. R. Belić, "Anderson localization of light near boundaries of disordered photonic lattices," Phys. Rev. A **83**, 033813 (2011).
25. D. M. Jović, M. R. Belić, and C. Denz, "Transverse localization of light in nonlinear photonic lattices with dimensionality crossover," Phys. Rev. A **84**, 043811 (2011).
26. Y. Lahini, A. Avidan, F. Pozzi, M. Sorel, R. Morandotti, D. N. Christodoulides, and Y. Silberberg, "Anderson localization and nonlinearity in one-dimensional disordered photonic lattices," Phys. Rev. Lett. **100**, 013906 (2008).
27. Y. Lahini, R. Pugatch, F. Pozzi, M. Sorel, R. Morandotti, N. Davidson, and Y. Silberberg, "Observation of a localization transition in quasiperiodic photonic lattices," Phys. Rev. Lett. **103**, 013901 (2009).
28. E. Maciá, "The role of aperiodic order in science and technology," Rep. Prog. Phys. **69**, 397–441 (2006).
29. S. Longhi, "Discrete diffraction and shape-invariant beams in optical waveguide arrays," Phys. Rev. A **79**, 033847 (2009).

Journal of Biomedical Optics 19(12), 127005 (December 2014)

Single-beam, dual-view digital holographic interferometry for biomechanical strain measurements of biological objects

Dejan V. Pantelić,* Dušan Ž. Grujić, and Darko M. Vasiljević
University of Belgrade, Institute of Physics, Pregrevica 118, Zemun 11080, Belgrade, Serbia

Abstract. We describe a method for dual-view biomechanical strain measurements of highly asymmetrical biological objects, like teeth or bones. By using a spherical mirror, we were able to simultaneously record a digital hologram of the object itself and the mirror image of its (otherwise invisible) rear side. A single laser beam was sufficient to illuminate both sides of the object, and to provide a reference beam. As a result, the system was mechanically very stable, enabling long exposure times (up to 2 min) without the need for vibration isolation. The setup is simple to construct and adjust, and can be used to interferometrically observe any object that is smaller than the mirror diameter. Parallel data processing on a CUDA-enabled (compute unified device architecture) graphics card was used to reconstruct digital holograms and to further correct image distortion. We used the setup to measure the deformation of a tooth due to mastication forces. The finite-element method was used to compare experimental results and theoretical predictions. [DOI: 10.1117/1.JBO.19.12.127005]

Keywords: digital holography; interferometry; aberration correction; finite element method; dentistry.

Paper 140481R received Aug. 27, 2014; accepted for publication Nov. 10, 2014; published online Dec. 17, 2014.

1 Introduction

It is commonly perceived that a hologram records the full, three-dimensional (3-D) image of an object. In reality, the size and the position of the holographic plate relative to the object determine the content of the hologram. In this sense, a hologram is a fixed "window" onto the virtual, 3-D world. The holographic plate is an aperture through which to observe an object from a limited angular range perspective, without the possibility of "walking around" the hologram to observe its more distant side. The problem is even more pronounced in digital holography, which is limited by the small dimensions of CCD/CMOS chips (compared to classical holographic plates) and an inability to display a true 3-D image on the computer monitor.

The ability to see an object (especially a very asymmetrical one) from all directions can be important for some applications. Holographers have tried to record "walk-around" holograms, particularly for display holography. That involved bending the holographic film so as to surround the object, thereby widening the observation "window". Cylindrical[1,2] (e.g., Cross Lloyd's famous "kiss" hologram[3]), conical,[4] alcove,[5] and disk-type[6] holograms are well known in this context.

The problem of observation from multiple-viewpoints was also tackled by other means, usually involving a finite number of viewpoints. One approach uses additional computer processing in digital holography.[7] Another approach uses several observation angles with appropriate processing for use in a digital holographic microscopy[8] or holographic particle image velocimetry.[9]

The problem of viewing an object from several perspectives also exists in holographic interferometry. Unfortunately, the above approaches are not readily applicable and other techniques have been used so far. Transparent objects have been successfully analyzed using scatter plates or by probing with several beams.[10] A dual-channel holographic interferometer, with holographic optical elements, was proposed for the study of phase objects.[11] Opaque objects have been surrounded by flat mirrors to achieve separate views.[12] However, the typical distances between the images and the object in such arrangements are problematic for digital holography because of the spatial-frequency limitation of the charge-coupled device (CCD) detectors.

Full-view observations are also problematic in the field of biomechanics, where objects of interest are often very asymmetrical. Numerous techniques have been used such as moiré,[13] speckle interferometry,[14] and holography.[15] Usually, they reveal surface deformations while internal stresses remain hidden and require mathematical modeling using the finite-element method (FEM). Holography has been extensively used to observe minute tissue deformations under mechanical stress.[16,17] We previously described a dual-beam off-axis holographic interferometry method that used a single spherical mirror to simultaneously observe the front and rear of a tooth model.[18] The mirror produced a real, strongly distorted, image of the object placed at the center of curvature.

Here, we present a digital holographic method that uses a spherical mirror and a single expanded laser beam to observe and to illuminate an object from both sides while also generating the reference beam. The setup has excellent mechanical stability, because all the necessary beams are generated from the same input beam as in the local-reference beam configuration.[19] Our proposed technique can also be regarded as an extension and improvement of single-beam holography,[20] one of the simplest holographic methods. The digital nature of the method enables correction of image distortion and avoids wet chemistry. The

*Address all correspondence to: Dejan V. Pantelić, E-mail: pantelic@ipb.ac.rs

0091-3286/2014/$25.00

technique is generally applicable and can be used for holographic interferometry on any object of dimensions that are limited by the diameter of the spherical mirror.

To demonstrate the capabilities of the proposed technique, we present an interferometric measurement of tooth deformation resulting from mastication. A tooth is inherently asymmetrical, and we reveal the deformation-field asymmetry in the holographically generated interference images. We used a digital tooth model and the FEM to calculate the resulting deformation and for comparison with experiments.

2 Experimental Technique

The paraxial image of an object placed in front of a concave spherical mirror is formed according to a well-known spherical mirror equation. In particular, if the object is positioned at the center of curvature the image appears at the same distance from the mirror. The image is inverted, real, and has unit magnification. This configuration was used throughout our experiments.

As an illustration, Fig. 1(a) shows several rays incident on a tilted concave spherical mirror (M). An arbitrary object (O) is positioned at the center of curvature (R). Rays 3 to 6 clearly illuminate the front surface of the object and the scattered radiation can be directly captured by an observer (or detector S). Some of the rays (7 to 10) that miss the object and are reflected from the mirror illuminate the object from the rear. The scattered radiation is again reflected by the mirror, and produces an image (O') of the back side of the object. The rays that miss both the front and the rear side (i.e., 1, 2, and 11 to 20) continue to propagate, and are used as a reference beam in a holographic experiment.

In our experiment, we used a CW diode-pumped Nd-YAG laser operating at the second harmonic (532 nm wavelength, 100 mW power) to illuminate the object. The coherence length of the laser was 100 m, but a short-coherence laser (e.g., He-Ne) can also be used, because the path length difference between the object and the reference beams is of the order of several centimeters. The laser beam was expanded by a diverging lens and used to fill the aperture of the spherical mirror (aperture diameter 75.3 mm, radius of curvature 46 mm, and focal length 23 mm). Mirror quality is not very important; in fact, we used a mirror from an old projection device. The short focal distance strongly distorts the mirror image, as seen in the photograph (Fig. 2). For small objects (of the order of 1 cm), the distortion is weak and the setup is adequate. Larger objects require computer-based compensation of the aberration to yield meaningful measurements. This procedure will be described in detail in the next section.

A digital single-lens reflex camera (Canon EOS50d, with an APS-C CMOS sensor with 14-bit dynamic range, 25.1 × 16.7 mm dimensions, and a 4752 × 3168 image size) recorded

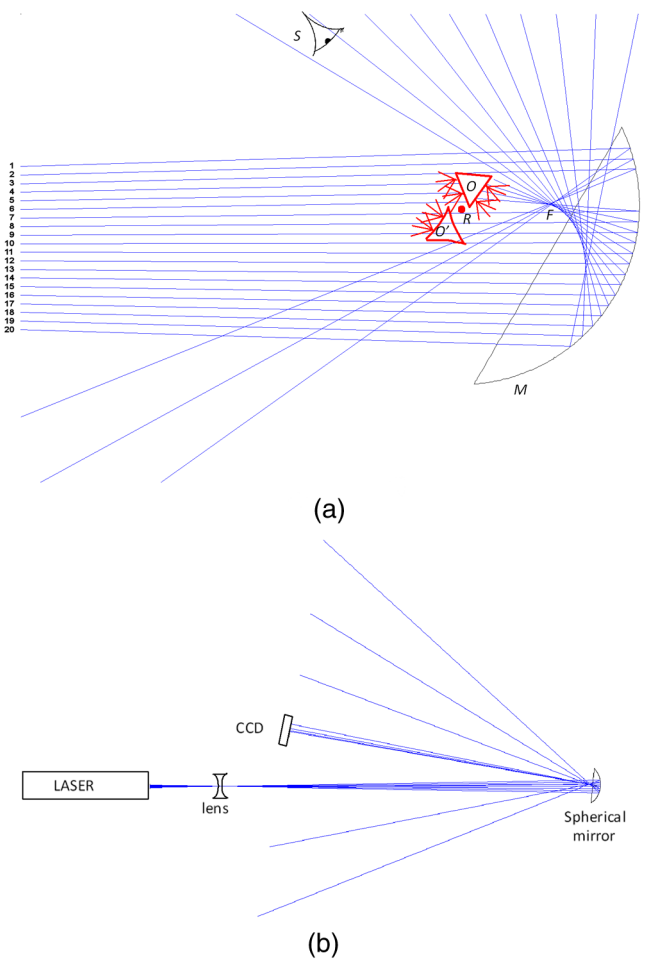

Fig. 1 (a) An object (O) is placed at a distance $2f$ from the spherical mirror (M) (f– focal distance) and its image is formed at O'. R is the center of curvature, F is the focal point of the beams reflected from the mirror, and S is observation (detection) direction; (b) the experimental setup.

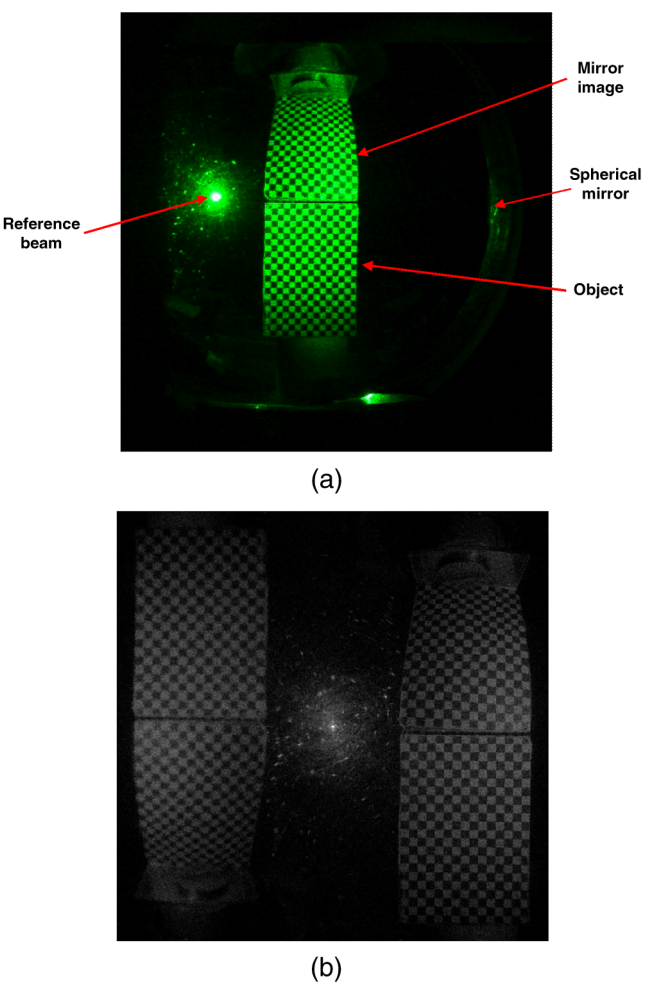

Fig. 2 (a) Photograph of a test object: a flat plate, checkered on both sides (down), its mirror image (up), and the reference beam (left). (b) Holographic reconstruction of the test object.

the holograms, in either RAW or JPG format, before further processing by computer. The setup is schematically presented in Fig. 1(b).

The object is positioned as previously described [Fig. 1(a)], but with a slight displacement from the optical axis to avoid blocking its own image (i.e., O and O' do not overlap). Finally, an observer simultaneously sees the object O, its mirror image O', and a reference beam, produced by the laser beam being focused by the mirror [see photograph in Fig. 2(a)].

Several other factors must be taken into account when generating the hologram. The most important is the distance between the object and the CCD camera, which should be such that the spatial frequencies of the hologram can be resolved by the CCD chip (e.g., a 4.7-μm inter-pixel distance for an EOS 50d camera). In our setup, the distance must be larger than approximately 0.7 m. Another issue is the reference-to-object beam ratio for achieving a deep modulation of the holographic interference pattern. In our experience, this is not critical as the dynamic range of a detector is high (14 bit). If necessary, we placed an additional neutral density filter in the reference beam to better adjust the reference-to-object beam intensity ratio. Most of the time, we used the setup without additional optical components.

The final holograms, having 4752×3168 pixels, were transferred to a computer and numerically processed on a CUDA-enabled graphics card (NVidia GeForce 560Ti) using a computational wave optics (CWO) software package[21] (under the computer physics communications program library CPC nonprofit use license agreement,)[22] for parallel processing. A holographic reconstruction of the test object in Fig. 2(a) is shown in Fig. 2(b). The zeroth diffraction order is in the middle and the useful orders are visible on the left and right. A shifted Fresnel algorithm[23] was mainly used, allowing the efficient separation of the useful diffraction order from the other two. This kind of algorithm enables shifting of the reconstruction window with respect to the hologram, while the window size can be arbitrarily chosen. The algorithm is applicable to long propagation distances. For distortion correction, in addition to the shifted Fresnel algorithm, we had to use the convolution-type (angular frequency[21]) algorithm, which is valid for short propagation distances.

3 Computational Correction of the Image Distortion

Aberration correction is most usually directly performed in an optical system using additional optical components, and making it complicated and costly. On the other hand, digital holography is an ideal ground for digital aberration correction, since both the phase and the amplitude of the optical field are known.[24] In our case, the image is sharp, but distorted. We solved the problem by digitally backpropagating the image through the spherical mirror all the way to the object location.

The simplified geometry of the spherical mirror imaging system is shown in Fig. 3. As explained above, spherical mirror M produces an image I_B of the object backside O_B [Fig. 3(a)]. The hologram was recorded and reconstructed to simultaneously reveal the image of the front (O_F) and the distorted image (I_B) of the back. The distortion of image I_B was corrected by reversing the propagation direction of the corresponding wave field and reflecting it off the mirror [Fig. 3(b)].

The exact calculation of the distortion compensation is more complicated than it seems. This is a consequence of the variable

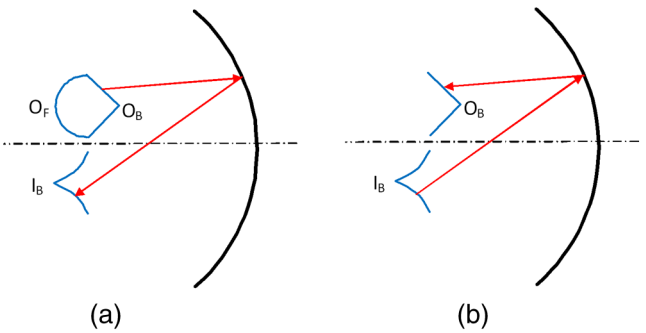

Fig. 3 (a) The backside (O_B) of an object produces a distorted image (I_B) after reflecting from the spherical mirror. (b) The aberration is software-compensated by backpropagating the reconstructed wavefront.

magnifications across the field of an imaging system.[25] To demonstrate this in our particular case, we consider an annular section of the mirror, as shown in Fig. 4. A light field propagates and reflects from the annulus. The process is mathematically described as a multiplication of the field with a corresponding phase factor. Generally speaking, the phase factor is complicated[26] but can be approximated to a spherical wavefront. Within this approximation, the annulus focuses the wavefront to the point F in Fig. 4. Considering the annulus as a simple spherical mirror with radius of curvature R, it follows that its focal distance f (equal to the radius of the reflected spherical wavefront) varies with height h as

$$f = \sqrt{R^2 - h^2} - \frac{R^2}{2\sqrt{R^2 - h^2}}. \tag{1}$$

Thus, the required phase factor is a spherical wavefront with radius f.

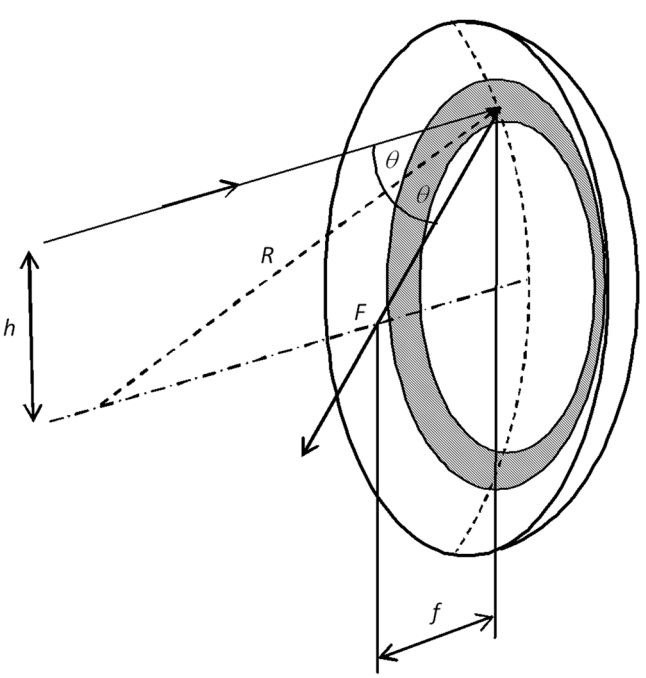

Fig. 4 The focal length f of an annular section of the mirror depends on the height h and the mirror radius of curvature R.

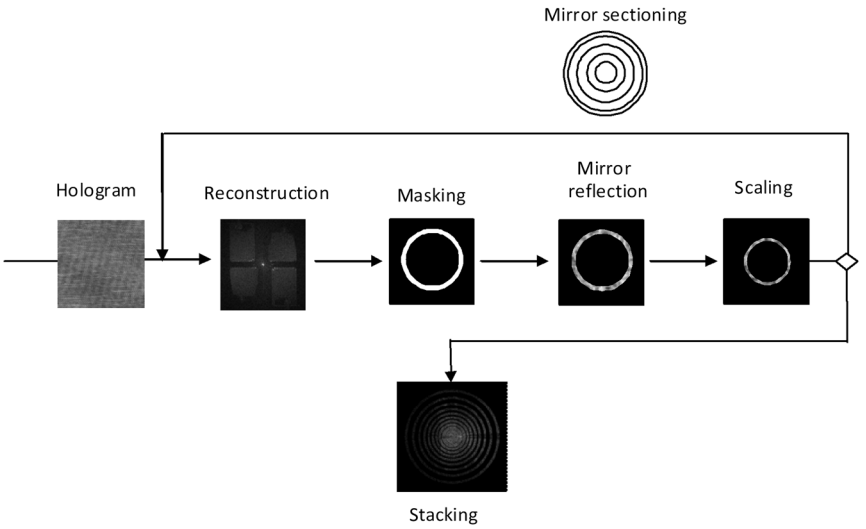

Fig. 5 Schematic of the distortion-correction procedure. A mirror is divided into annular sections, and the wavefront is backpropagated through each section.

To solve the complete problem, a given mirror is divided into a set of annular sections and the problem is analyzed section by section. The hologram is reconstructed and a wavefront propagates to each section. The field is masked by the corresponding annular aperture and is multiplied by the appropriate spherical phase factor before propagating back to the image plane. The whole procedure is summarized in Fig. 5, and mathematical details are given in the Appendix.

We verified the method by using the test object shown in Fig. 2: a plate, checkered on both sides with 1 mm squares. A hologram was recorded as described in Sec. 2, and a single-diffraction order was extracted [Fig. 6(a)], where the object and its (distorted) mirror image are seen one above the other. The image resulting from the distortion correction is shown in the upper part of Fig. 6(b). The final result is a set of two images that contain the complete dual-view information on the object [red squares in Figs. 6(a) and 6(b)].

It is important to note that the complete phase information is preserved during distortion correction. This means that distortion correction can be applied to holographic interferograms. To verify this possibility, we used another test object [a rectangular aluminum block with a blind hole—Fig. 7(a)] that could be mechanically loaded using a brass tool with a spherical tip (sphere diameter 5.5 mm). Two holograms were recorded for the unloaded and loaded objects. The resulting interferogram is shown in Fig. 7(b). Its distortion-corrected version is shown in Fig. 7(c).

The distortion-correction process is notably time consuming, as the Fresnel transform must be performed several times. A high-quality reconstruction requires the reconstructed image to be divided into 40 to 80 circular sections (as described in Sec. 3). The Fresnel transform must be performed twice for each section: the first transform is of the "shifted Fresnel" type,[23] and the second transform is of the "angular spectrum" type.[21] We used parallel computing on a graphics card, and the image reconstruction from a hologram (2048×2048 pixels) lasts 2.5 s, without distortion correction. The correction process is more time consuming and lasts up to 2 min, depending on the number of sections used through the process.

4 Finite-Element Modeling of Dental Tissue

Our aim was to use the holographic technique (described in Secs. 2 and 3) to measure deformations in dental tissue due to mastication forces. In order to calculate internal stresses, we had to develop a realistic FEM model of a tooth.

We used a human upper second premolar that had been extracted for orthodontic reasons. The tooth was scanned using

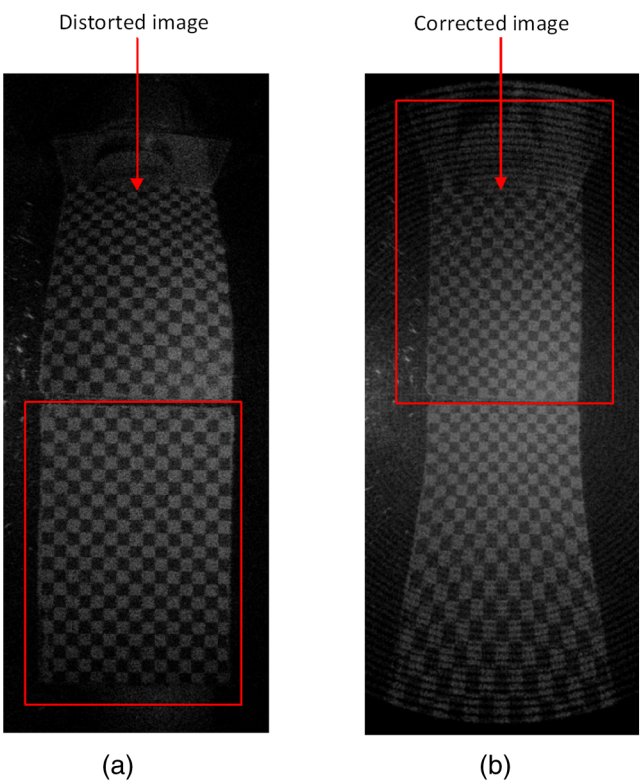

Fig. 6 (a) Single-diffraction order of a reconstructed digital hologram, containing an object (bottom) and its spherical mirror image (top). (b) Distortion-corrected diffraction order. The red squares contain the complete dual-view information about the object.

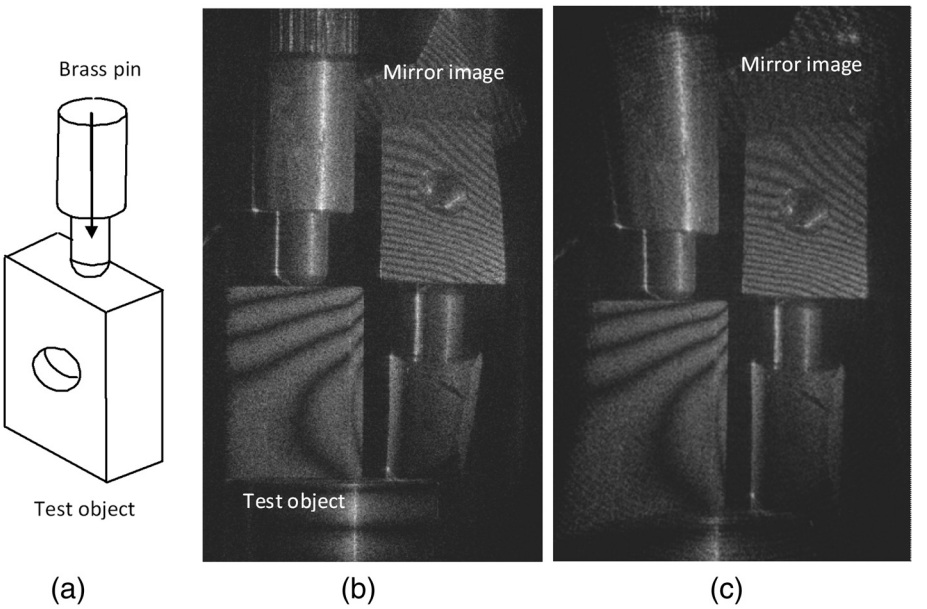

Fig. 7 (a) Diagram of a test object (aluminum block with a blind hole) and a brass loading tool, (b) digital holographic interferogram of the test object, (c) distortion-corrected interferogram. Due to high dynamic range of the resulting image, the intensity scale is logarithmic.

a 64-slice CT scanner (Sensation 64 Cardiac CT, manufactured by Siemens, Germany). Forty-two slices were sufficient to acquire the whole tooth with a 0.5 mm resolution between consecutive slices. Within each slice, we were able to resolve 110 × 88 pixels with a 0.1 mm resolution.

This set of slice images was the starting point for creating a 3-D solid model. All images were segmented by applying an intensity threshold to identify the boundaries among the enamel, dentin, and pulp regions. One of the slices and its corresponding segmented image are given in Figs. 8(a) and 8(b), respectively. The result was saved as a series of data files in drawing exchange format in order to facilitate importing into a 3-D solid modeling program.

The 3-D solid model was constructed by first defining contours using splines, and then building the 3-D solid body from the set of splines. The procedure was repeated for each tooth structure: the enamel, the dentin, and the pulp. The resulting 3-D solid model of the whole human maxillary premolar is displayed in Fig. 9.

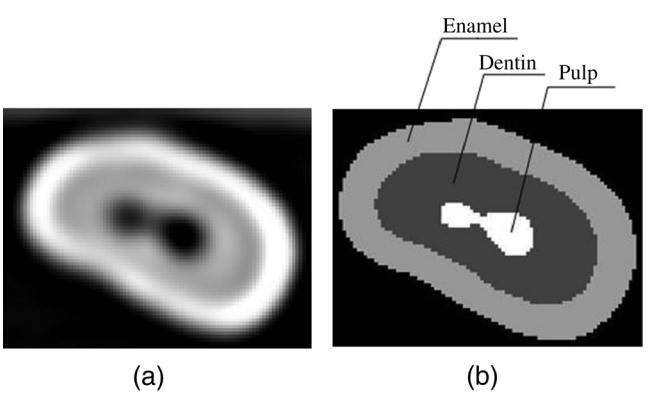

Fig. 8 (a) One CT slice of a human upper second premolar tooth. (b) The corresponding segmented image.

In order to calculate the various types of stress and strain using the FEM, the fixture, the load, and the mesh had to be defined. The exterior nodes on the dentin surface were fixed in all directions and could neither translate nor rotate. A load was applied at the two points on the cusps indicated by green arrows in Fig. 9(b). Parabolic tetrahedral solid elements (defined by four corner nodes, six mid-side nodes, and six edges) were used for meshing, as they more accurately represent

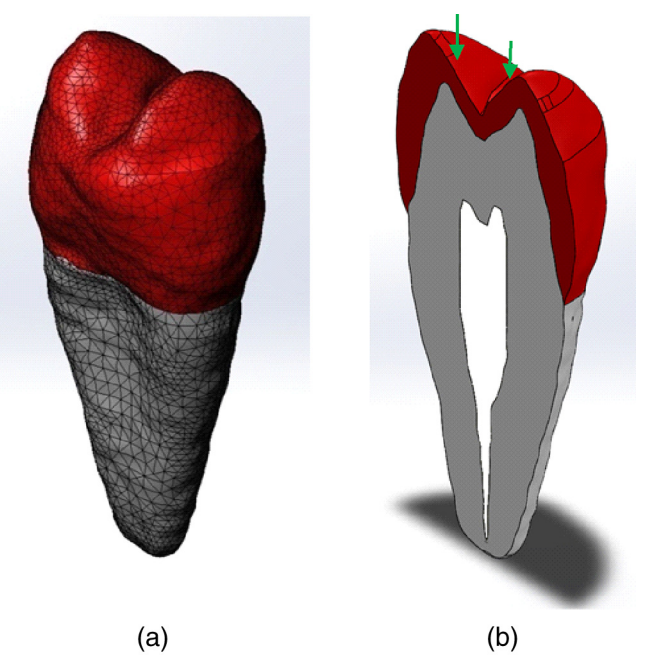

Fig. 9 Three-dimensional (3-D) solid model of a human maxillary premolar: (a) a meshed model and (b) its cross section (red–enamel, gray–dentine, white–pulp, green arrows indicate application points mechanical forces).

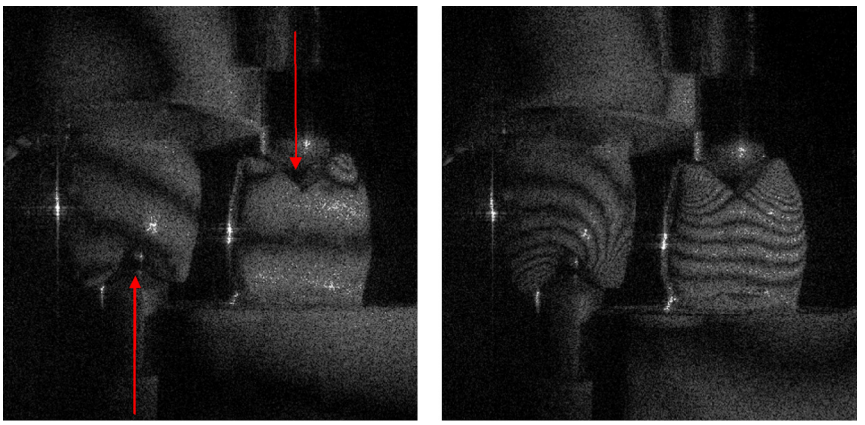

Fig. 10 Interferograms of an artificial tooth under (a) 100 N and (b) 250 N loads applied by a brass tool. The red arrows indicate the load directions. Due to high dynamic range of the resulting image, the intensity scale is logarithmic.

curved boundaries. The final 3-D model had 174,196 nodes and 118,126 elements.

5 Dual-View Measurement of Masticatory Effects Using Holographic Interferometry

We analyzed a problem of stress and strain acting on a single tooth during mastication. The results, obtained by dual-view holographic interferometry (as described in Secs. 2 and 3), were compared with the FEM (see Sec. 4).

Experiments were performed using a physical model of a tooth obtained by rapid prototyping (one possible method for fabricating a substitute for a human tooth in dental research).[27] The digital 3-D model was used as the input for a 3-D printer to generate a plastic copy of a real tooth. The mechanical properties of the resulting model certainly do not match those of the original (the elastic modulus of dentin is 7 to 46 GPa, that of enamel 80 to 1800 GPa,[28] compared with 2.5 GPa for the plastic model), but can be used to assess correspondences between the numerical FEM model and experimental results. An additional advantage is the availability of many samples with no medical or ethical implications.

The tooth model was mounted in a hollow aluminum cylinder and permanently fixed with dental gypsum. The root was completely embedded in the gypsum, while the entire tooth crown was visible and accessible to holographic measurements. A brass tool with a spherical head (shown schematically in Fig. 7(a), similar to that in Ref. 29) was used to controllably apply force to the tooth. The force was directed along the long tooth axis (red arrow in Fig. 10) and its magnitude was measured with a force gauge. The tooth was positioned in front of a spherical mirror, as previously described. A reference hologram was recorded with no force applied. As the force was then varied between 20 and 250 N, corresponding holograms were recorded, and interferograms were calculated (two examples shown in Fig. 10). We would like to note that the phase difference information could be useful in some instances, such as contouring. In our case, classical interferograms were enough to test the correspondence between the experiment and FEM modeling.

From the computational point of view, the digital tooth model has uniform mechanical properties [as shown in Fig. 11(a)], corresponding to the physical model manufactured by 3-D printing. The loading configuration is shown in Fig. 11(b), where the tool orthogonally acts to tooth cusps, imitating the experimental configuration. The force was varied within the experimental range (20 to 250 N). The computational results are shown in Figs. 12(a) and 12(b), where the deformation on both sides of a tooth can be seen, encoded by pseudocolors. It is not possible to completely replicate the intricate shape of a tooth and determine the position of contact points between the tooth and the pressing tool, as well as the direction of the force. Taking all that into account, FEM modeling reproduces reasonable experimental results.

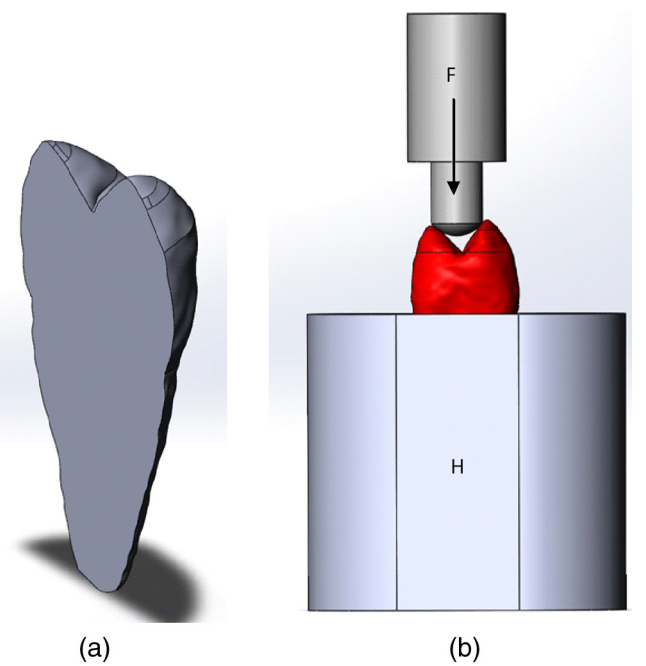

Fig. 11 (a) Cross section of a finite-element model (FEM) with uniform mechanical properties corresponding to a physical tooth model manufactured by rapid prototyping. (b) A tooth model mounted in a holder (*H*), with a spherical-tip loading tool (*F* is an externally applied force).

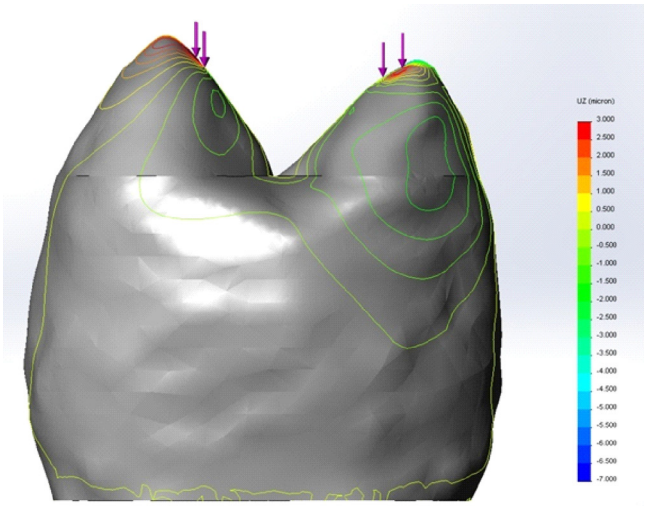

(a)

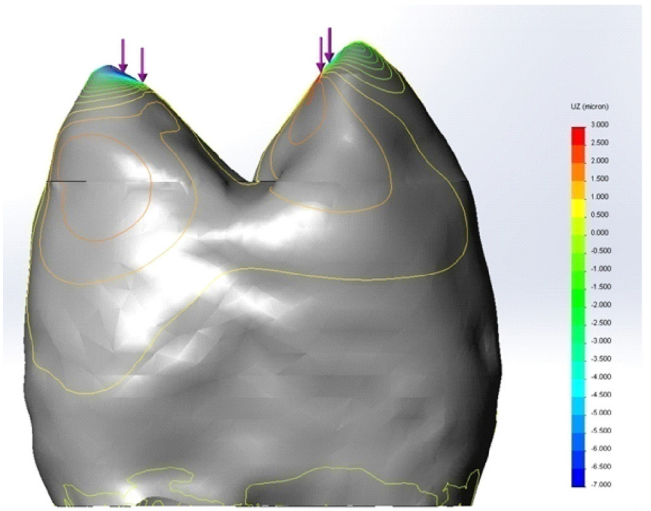

(b)

Fig. 12 Simulated deformation of an artificial tooth, calculated using FEM: (a) front side, (b) back side.

6 Discussion and Conclusions

The technique described in this study is universally applicable, but several points should be taken into account. First, we found that the method can be used without aberration correction if the object is smaller than approximately one-third of the mirror aperture. Under this condition, distortion is negligible and no corrections are needed. The image of larger objects becomes strongly distorted near the edge of the aperture (see Fig. 2) and requires numerical compensation as previously described. By using larger mirrors (of 15 to 20 cm diameter), objects with a size of the order of 5 cm could be investigated.

The mechanical stability of the whole system is excellent, since the reference and object beams are generated from the same illuminating beam. Therefore, moving the illuminating beam similarly affects both the reference and object beams. Consequently, the interference pattern is negligibly perturbed provided the beam deviation is not too large. In practice, holograms were recorded on an optical table without any vibration isolation and the camera was mounted on a tripod placed on the ground (away from the table); yet, the holograms produced were of excellent quality. To directly test the stability more, we deliberately reduced the laser beam

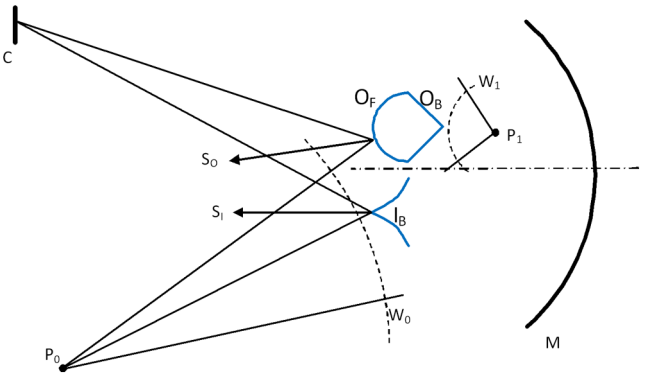

Fig. 13 Sensitivity vectors S_O and S_I of an object and its mirror image, respectively. M is the spherical mirror, P_0 an illumination source, W_0 the corresponding wavefront, P_1 the conjugate mirror image of P_0, and W_1 the corresponding wavefront. O_F and O_B are the front and back sides of the object, respectively, and I_B is the mirror image of the back side O_B. C is the camera detector.

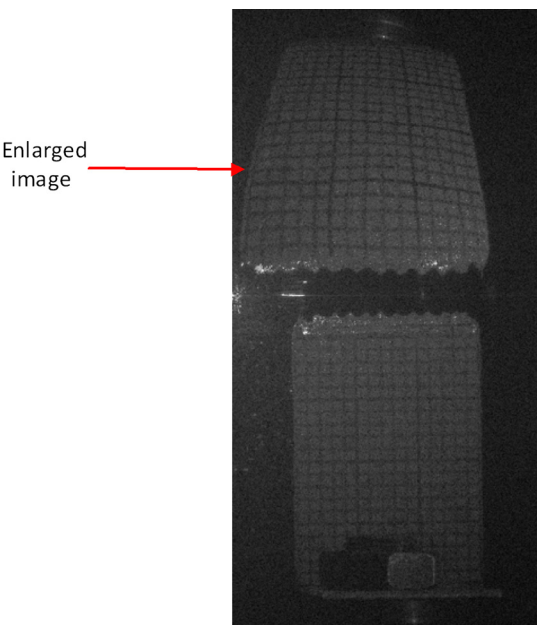

Fig. 14 Enlarged back side of an object.

intensity in order to increase the exposure. We were able to record high-quality holograms even for an exposure time of 2 min.

Interpreting fringes requires an estimation of the sensitivity vector.[30] This is simple in the case of the object itself (its front side O_F in Fig. 13), because the sensitivity vector (S_O) simply bisects the angle between the illumination and observation directions. This vector is fairly constant since the object is small, the curvature radius of the object beam is large, and the observation direction is fixed by the position of the camera chip (C). The situation is more complicated with the mirror image I_B and its associated sensitivity vector. First, we have to note that the back-side O_B is illuminated with the wavefront W_1. It is generated by the point source P_1, which is conjugate to the illuminating source P_0. The conjugate mirror images of O_B, W_1, and P_1 are I_B, W_0, and P_0, respectively, and this is what we observe in reality. We conclude that the sensitivity vector S_I of the mirror image is defined by the illumination direction P_0I_B and the observation direction CI_B. Again, the sensitivity vector S_I is constant, for the same reasons as for vector S_O.

An additional benefit of the method is the possibility to enlarge the image by simply moving the object closer to the mirror. Even though the distortion will be larger, it can be corrected by the algorithm described in Sec. 3. This allows more details to be observed, albeit on only one object surface (Fig. 14).

There are also small experimental issues. The illumination level of the object and its image should be approximately the same. By properly aligning and positioning the Gaussian illuminating beam, we achieved a sufficiently even illumination. If necessary, the part of the beam that illuminates the front can be easily filtered with a neutral density filter. It is required to mask stray radiation, as in almost any holographic setup. If more than two separate views are needed, additional spherical mirrors can be used.

In conclusion, we have simultaneously described a simple technique for observing the front and back sides of an object by holographic interferometry. Only one spherical mirror and a single laser beam are needed to illuminate the object from both sides and to produce a reference beam. The setup is mechanically very stable because it resembles that used in local reference beam techniques. The proposed method is versatile and can be adapted to many experimental situations, providing that the object is smaller than the mirror. We illustrated the benefits of the proposed scheme by performing holographic interferometry of the dental model manufactured by rapid prototyping.

Appendix: Mathematical Procedure and Algorithm for Distortion Correction

The principle of aberration correction is explained in Sec. 3 and schematically presented in Fig. 5. The mathematics discussed in this Appendix refers to Fig. 15.

For simplicity, all the following equations are one-dimensional, but can be straightforwardly rewritten in the proper two-dimensional form. Our calculations use a Fresnel integral defined as

$$U(x_2) = \frac{\exp\left(i\frac{2\pi}{\lambda z}\right)}{i\lambda z}\exp\left(i\frac{\pi}{\lambda z}x_2^2\right)\int_{-\infty}^{\infty} u(x_1) \times \exp\left(i\frac{\pi}{\lambda z}x_1^2\right)\exp\left(-i\frac{2\pi}{\lambda z}x_1x_2\right)\mathrm{d}x_1. \quad (2)$$

Propagation (distance z) from the hologram plane to the plane of the mirror section S_i is approximated by the following Fresnel integral (as the propagation distance is largely compared to the hologram dimensions)

$$u_0(x_z)=\exp\left(\frac{i\pi}{\lambda z}x_z^2\right)\int_{-\infty}^{\infty} u(x)\exp\left(\frac{i\pi}{\lambda z}x^2\right)\exp\left(-i\frac{2\pi}{\lambda z}x_z x\right)\mathrm{d}x. \quad (3)$$

This equation can be described as the product

$$u_0(x_z) = \exp\left(i\frac{\pi}{\lambda z}x_z^2\right)P(x_z), \quad (4)$$

of a quadratic (oscillatory) phase factor and an integral expression

$$P(x_z) = \int_{-\infty}^{\infty} u(x)\exp\left(i\frac{\pi}{\lambda z}\right)\exp\left(-i\frac{2\pi}{\lambda z}x_z x\right)\mathrm{d}x. \quad (5)$$

The resulting equation accurately describes the resulting field, except for the fact that the quadratic phase factor quickly oscillates and is aliased during computation (because of finite sampling). Therefore, the field distribution defined by u_0 [Eq. (4)] cannot be numerically propagated further without introducing

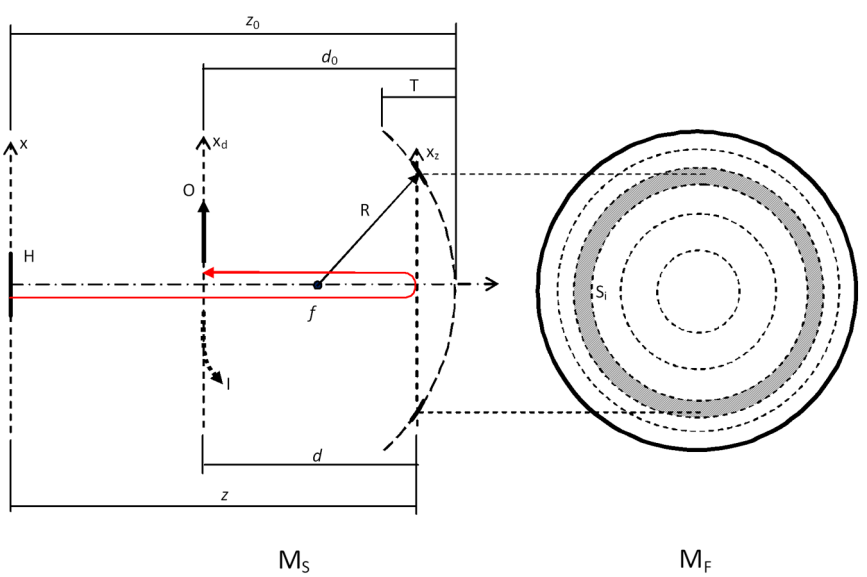

Fig. 15 Two orthogonal views (side view is on the left and front view is on the right) of the spherical mirror divided into a set of annular sections. *H*– a hologram (CCD chip), *I*– aberrated image, *O*– corrected image, *R*– mirror radius, x, x_d, and x_z are the hologram-plane, image-plane, and intermediate-plane locations, respectively. M_S– side view of the mirror, M_F– front view of a mirror, divided into a set of sections S_i. Symbols z, d, T, z_0, d_0 and are the geometrical dimensions and the propagation distances used in the calculations. The red arrow shows the order of wavefront calculations, starting from the hologram plane x, propagating to the intermediate plane x_z (containing the section S_i), and then backpropagating to the image plane x_d.

artifacts.[31] However, the integral itself [Eq. (5)] does not oscillate.

The wave is further reflected from the mirror and the field distribution, defined by Eq. (4), must be multiplied by the corresponding spherical phase factor

$$u_1(x_z) = \exp\left(i\frac{\pi}{\lambda f}x_z^2\right)u_0(x_z), \tag{6}$$

where f is the focal length of the mirror section. The reflected field, Eq. (6), further propagates a distance d to the image plane, and is then described by

$$u_2(x_d) = \exp\left(i\frac{\pi}{\lambda d}x_d^2\right)\int_{-\infty}^{\infty} u_1(x_z)\exp\left(i\frac{\pi}{\lambda d}x_z^2\right) \times \exp\left(-i\frac{2\pi}{\lambda d}x_d x_z\right)\mathrm{d}x_z. \tag{7}$$

By substituting u_1 [Eq. (6)] into Eq. (7) and using the relation between u_0 and $P(x_z)$ [Eq. (4)], we get

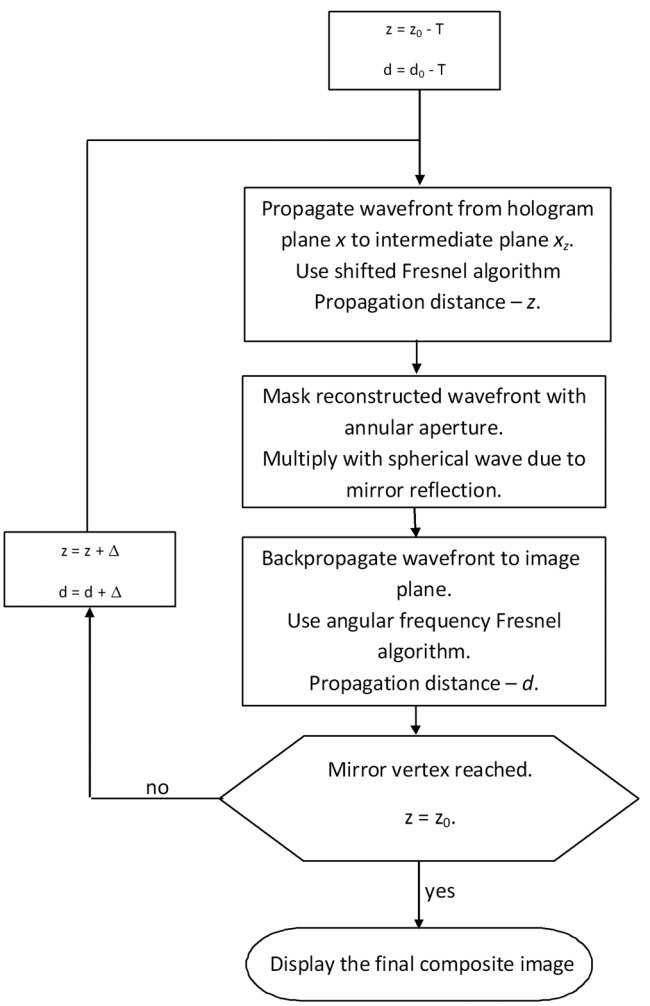

Fig. 16 A flow chart of a distortion-correction algorithm.

$$u_2(x_d) = \exp\left(i\frac{\pi}{\lambda d}x_d^2\right)\int_{-\infty}^{\infty} P(x_z)\exp\left(i\frac{\pi}{\lambda z}x_z^2\right) \times \exp\left(i\frac{\pi}{\lambda f}x_z^2\right)\exp\left(i\frac{\pi}{\lambda d}x_z^2\right)\exp\left(-i\frac{2\pi}{\lambda z}x_d x_z\right)\mathrm{d}x_z. \tag{8}$$

We define an equivalent propagation distance z_e with

$$\frac{1}{z_e} = \frac{1}{d} + \frac{1}{f} + \frac{1}{z}. \tag{9}$$

The diffraction integral [Eq. (8)] is then written more compactly as

$$u_2(x_d) = \exp\left(i\frac{\pi}{\lambda d}x_d^2\right)\int_{-\infty}^{\infty} P(x_z)\exp\left(i\frac{\pi}{\lambda z_e}x_z^2\right) \times \exp\left(-i\frac{2\pi}{\lambda d}x_d x_z\right)\mathrm{d}x_z. \tag{10}$$

Observe that the final integral is slightly different from the standard Fourier form of the Fresnel diffraction integral (1). The difference is in the exponential terms in the integrand, which should have the same constant factor $\pi/\lambda z$. To reduce the integral in Eq. (8) into a standard form [as in Eq. (2)], we scale the variable x_d as

$$x_d = \frac{z_e}{d}\xi, \tag{11}$$

and finally obtain the integral

$$u_2(\xi) = \exp\left(i\frac{\pi z_e^2}{\lambda d^3}\xi^2\right)\int_{-\infty}^{\infty} P(x_z)\exp\left(i\frac{\pi}{\lambda z_e}x_z^2\right) \times \exp\left(-i\frac{2\pi}{\lambda z_e}\xi x_z\right)\mathrm{d}x_z. \tag{12}$$

By separating the quadratic phase factor and the integral, we get

$$u_2(\xi) = \exp\left(i\frac{\pi z_e^2}{\lambda d^3}\xi^2\right)P_1(\xi), \tag{13}$$

where

$$P_1(\xi) = \int_{-\infty}^{\infty} P(x_z)\exp\left(i\frac{\pi}{\lambda z_e}x_z^2\right)\exp\left(-i\frac{2\pi}{\lambda z_e}\xi x_z\right)\mathrm{d}x_z. \tag{14}$$

The result of the above integral must be scaled from ξ back to the physical coordinates x_d using Eq. (11). During the calculations only the integrals need to be calculated [P in Eq. (5) and P_1 in Eq. (14)]; the quadratic phase factor in Eq. (13) may be subsequently included if necessary.

From the numerical point of view, we started the process by calculating the integral in Eq. (5). In effect, we reconstructed the hologram at a distance z, but omitted the quadratic phase factor. The propagation distance was large and a Fourier form of the Fresnel transform algorithm was used.[21] The resulting far-field was masked with an annular mask, and was further propagated using Eq. (14), which includes three quadratic phase factors (combined into an equivalent propagation distance z_e [Eq. (9)]. In this step, the propagation distance was short and

a convolution-type (angular frequency[21]) algorithm was used. Finally, the resulting ring-like image was rescaled according to Eq. (11). The whole process was repeated for all the mirror sections, and a set of ring-like images was obtained. These were coherently summed to produce a final distortion-corrected image (with a correction applied to both the phase and amplitude). The whole procedure is visualized in Fig. 5, and the appropriate algorithm flow chart is shown in Fig. 16.

The software was written in C++, based on a previously described algorithm. The CWO library[21] was used to speed up the computation by using parallel processing on a graphics card.

Acknowledgments

This research was funded by the Serbian Ministry of Education, Science, and Technological Development, under the Contract Nos. ON171038 and III45016. We express our gratitude to Professor Dr. Larisa Blažić, Ivana Kantardžić, and Tatjana Vukadinov, from the University of Novi Sad, Faculty of Medicine, Dental Clinic, Serbia, for helping us with CT scanning of a tooth and three-dimensional (3-D) model construction.

References

1. Y. S. Cheng and R. C. Chang, "Image-plane cylindrical holographic stereogram," *Appl. Opt.* **39**, 4058–4069 (2000).
2. O. D. D. Soares and J. C. A. Fernandes, "Cylindrical hologram of 360° field of view," *Appl. Opt.* **21**, 3194–3196 (1982).
3. S. F. Johnston, *Holographic Visions, a History of New Science*, Oxford University Press, Oxford, United Kingdom (2006).
4. K. Okada et al., "Conical holographic stereograms," *Opt. Commun.* **73**, 347–350 (1989).
5. S. Benton, "Real image holographic stereograms," U.S. Patent No. 4834476 (1989).
6. Y.-S. Cheng, Z.-F. Chen, and C.-H. Chen, "Virtual-image generation in 360 degree viewable image-plane disk-type multiplex holography," *Opt. Express* **21**, 10301–10313 (2013).
7. J. Maycock et al., "Reconstruction of partially occluded objects encoded in three-dimensional scenes by using digital holograms," *Appl. Opt.* **45**, 2975–2985 (2006).
8. Y. Takaki and H. Ohzu, "Hybrid holographic microscopy: visualization of three-dimensional object information by use of viewing angles," *Appl. Opt.* **39**, 5302–5308 (2000).
9. J. Sheng, E. Malkiel, and J. Katz, "Single beam two-views holographic particle image velocimetry," *Appl. Opt.* **42**, 235–250 (2003).
10. R. Jones and C. Wykes, *Holographic and Speckle Interferometry*, Cambridge University Press, Cambridge, United Kingdom (1989).
11. A. K. Sharma et al., "A holographic dual-channel interferometer," *Curr. Sci.* **91**(3), 269–271 (2006).
12. R. K. Erf, "Solid propellent rocket inspection," in *Holographic Nondestructive Testing*, R. K. Erf, Ed., pp. 365–372, Academic Press, New York, London (1974).
13. J. D. Wood et al., "Mapping of tooth deformation caused by moisture change using moiré interferometry," *Dent. Mater.* **19**, 159–166 (2003).
14. L. Yang et al., "Measurement of strain distributions in mouse femora with 3-D-digital speckle pattern interferometry," *Opt. Lasers Eng.* **45**, 843–851 (2007).
15. S. M. Solís, F. M. Santoyo, and M. del Socorro Hernández-Montes, "3-D displacement measurements of the tympanic membrane with digital holographic interferometry," *Opt. Express* **20**, 5613–5621 (2012).
16. G. Caroena et al., "Mastication effort study using photorefractive holographic interferometry technique," *J. Biomech.* **43**, 680–686 (2010).
17. D. Pantelić et al., "Real-time measurement of internal stress of dental tissue using holography," *Opt. Express* **15**, 6823–6830 (2007).
18. D. Pantelić et al., "Holographic measurement of a tooth model and dental composite contraction," *Mater. Manuf. Processes* **24**, 1142–1146 (2009).
19. H. J. Caulfield, "Information retrieval from local reference beam holograms," *Phys. Lett.* **27A**, 319–320 (1968).
20. P. Hariharan, *Basics of Holography*, Cambridge University Press, Cambridge, United Kingdom (2002).
21. T. Shimobaba et al., "Computational wave optics library for C++: CWO ++ library," *Comput. Phys. Commun.* **183**, 1124–1138 (2012).
22. The computer physics communications program library CPC nonprofit use license agreement, http://cpc.cs.qub.ac.uk/licence/licence.html.
23. R. P. Muffoletto, J. M. Tyler, and J. E. Tohline, "Shifted Fresnel diffraction for computational holography," *Opt. Express* **15**, 5631–5640 (2007).
24. T. Colomb et al., "Numerical parametric lens for shifting, magnification, and complete aberration compensation in digital holographic microscopy," *J. Opt. Soc. Am. A* **23**, 3177–3190 (2006).
25. F. A. Jenkins and H. E. White, *Fundamentals of Optics*, McGraw-Hill Companies, New York (2001).
26. E. Román-Hernández et al., "Wavefronts and caustics of a spherical wave reflected by an arbitrary smooth surface," *J. Opt. Soc. Am. A* **26**, 2295–2305 (2009).
27. G. H. Yassen, J. A. Platt, and A. T. Hara, "Bovine teeth as substitute for human teeth in dental research: a review of literature," *J. Oral Sci.* **53**, 273–282 (2011).
28. N. Meredith et al., "Measurement of the microhardness and Young's modulus of human enamel and dentine using an indentation technique," *Archs. Oral Biol.* **41**, 539–545, (1996).
29. P. V. Soares et al., "Influence of restorative technique on the biomechanical behavior of endodontically treated maxillary premolars. Part II: strain measurement and stress distribution," *J. Prosthet. Dent.* **99**, 114–122 (2008).
30. T. Kreis, *Handbook of Holographic Interferometry: Optical and Digital Methods*, Willey-VCH, Weinheim, Germany (2004).
31. D. Mas et al., "Fast numerical calculation of Fresnel patterns in convergent systems," *Opt. Commun.* **227**, 245–258 (2003).

Dejan V. Pantelić received his PhD degree in physics from the University of Belgrade, Serbia. He is a professor at the Photonics Center, Institute of Physics, University of Belgrade. His research interests include holography, microscopy, micro-optics, and biophotonics. He is a member of the Optical Society of America.

Dušan Ž. Grujić is a PhD student and research assistant at the Photonics Center, Institute of Physics, Belgrade, Serbia. He received his MSc degree at the Department of Applied Physics and Informatics, Faculty of Physics, University of Belgrade, Serbia. His research interests include application of digital holography techniques for measuring small changes in fluids and solid materials, direct laser writing, using parallel data processing in numerical simulations.

Darko M. Vasiljević received his PhD degree in mechanical engineering from the University of Belgrade, Serbia, in 1998. Since 2000, he has been a professor of optical instruments and optoelectronics in mechanical engineering at the University of Belgrade. Since 2005, he is a full-time researcher at the Institute of Physics, University of Belgrade. His research interests include optical design of complex optical and optoelectronical systems, microlenses, holography, and biophotonics.

Phys. Scr. **T157** (2013) 014020 (3pp) doi:10.1088/0031-8949/2013/T157/014020

Zoom system for measurement of coherent backscattering of light in micro- and nanomaterials

D Pantelić, S Savić-Šević and D Grujić

Institute of Physics, University of Belgrade, Pregrevica 118, 11080 Zemun, Belgrade, Serbia

E-mail: pantelic@ipb.ac.rs

Received 18 August 2012
Accepted for publication 12 December 2012
Published 15 November 2013
Online at stacks.iop.org/PhysScr/T157/014020

Abstract
We report on an optical system capable of detecting backscattering cones within a wide angular range—from less than mrad up to 500 mrad. It is based on an intermediate optical system placed between the sample and the CCD camera equipped with a 5× zoom objective. The theory of operation is explained and experimental results are presented.

PACS numbers: 42.25.Fx, 42.25.Dd, 42.25.Kb

(Some figures may appear in color only in the online journal)

1. Introduction

Coherent backscattering is a process observed in physical systems with a certain amount of disorder. Systems can be either completely random (like clouds or milk) or regular with slight randomness. This is an interference phenomenon inherent for any type of wave—from electrons and sound to light. It is characterized by increased intensity in the exact backscattering direction. Coherent backscattering has been observed in many optical materials (artificial or natural) and gives important information about the mean free path of light, the density of scatterers and their dimensions.

Devices for the measurement of backscattering are simple in principle, but rather demanding from the experimental point of view [1]. The main problem is that the width of the backscattering cone is inversely proportional to the mean free path length of light. For materials with path lengths of the order of several micrometers (as in biological tissues) the cone is very narrow (of the order of microradians), while for nanostructured materials the backscattering cone can be quite wide (several hundreds of milliradians). In that respect, present systems are constructed for the observation of either wide [2] or narrow backscattering cones [3].

There are several experimental techniques for the detection of backscattered radiation. One of them is based on the angular scanning of a detector around the scattering sample. The technique is accurate but rather slow. An improvement is based on using many discrete detectors, in which case there is no need for mechanical scanning. However, the cost of such a system is high and there is the problem of achieving the same electrical response from all detectors. Another method is to use CCD array detectors and imaging optics, where the detection speed is significantly improved. However, a calibration procedure is needed to correct for variation of Fresnel losses inside the imaging system. None of those systems are capable of detecting both wide and narrow backscattering cones, thus significantly reducing their general utility.

Here we report on the universal system that can be used for both low and high backscattering angles. The system is based on imaging the scattering surface using an additional lens system. The image is directly projected into the entrance pupil of a zoom lens that is focused at infinity. In this way, the angular spectrum of scattered light is focused on the detection surface, making observation of the backscattering cone possible. In this configuration, the variable magnification of a zoom lens changes the angular field of view, depending on whether the backscattering cone is large or small. Light is detected on a 15.1 mega pixel resolution CMOS camera.

2. Principle of operation

In a classical imaging system for detection of backscattered radiation, the scattering sample is far from the entrance pupil of the imaging lens. Therefore, the angular range of scattered radiation is severely limited by the aperture

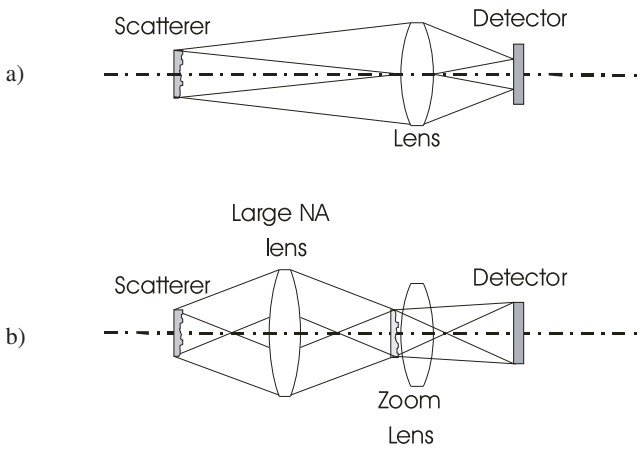

Figure 1. Schematic representation of (a) a classical imaging system for detection of backscattered radiation and (b) a zoom system for detection of backscattered radiation.

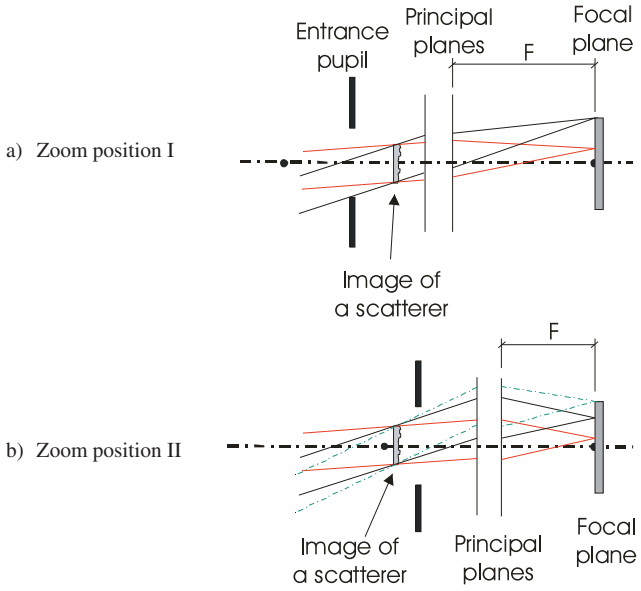

Figure 2. Imaging of the scatterer by a zoom system approximated with its principal and focal planes and entrance pupil: (a) long focal length and (b) short focal length.

diaphragm (figure 1(a)). Also the magnification of the system is constant.

The solution is to produce a real image of the scatterer (by an additional optical imaging system) and project it directly into the entrance pupil (figure 1(b)) of a lens in front of the detection plane. If a zoom lens is used before the detector then we have a variable magnification system, whose operation can be best understood by replacing a zoom lens by a set of principal and focal planes and an entrance pupil (figure 2).

Two zoom positions are presented in figure 2. The first zoom position is one with long focal length (figure 2(a)) in which a small angular range is observed on the whole detection area. The second zoom position is one with short focal length (figure 2(b)) in which a large scattering cone is projected on the detector surface. As can be seen, no matter how we change the focal length of a zoom lens, the image of a scatterer always stays close to the entrance pupil, thus significantly increasing the angular acceptance of the system.

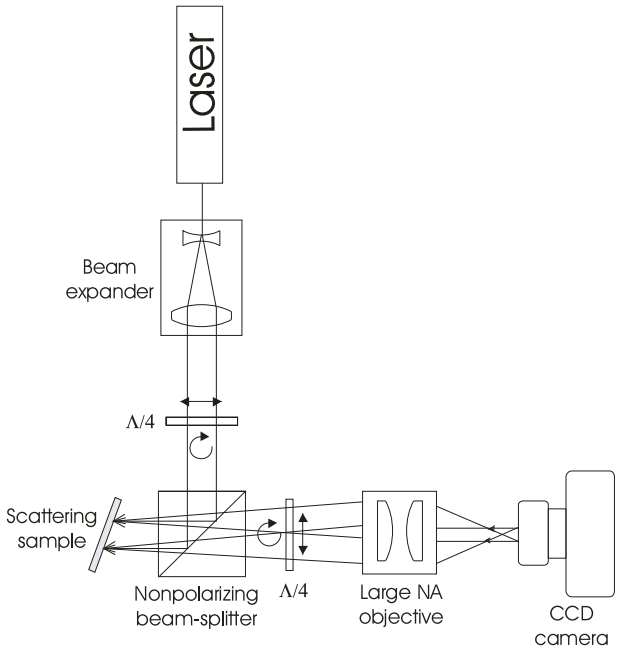

Figure 3. Experimental realization of a zoom system for detection of backscattered radiation.

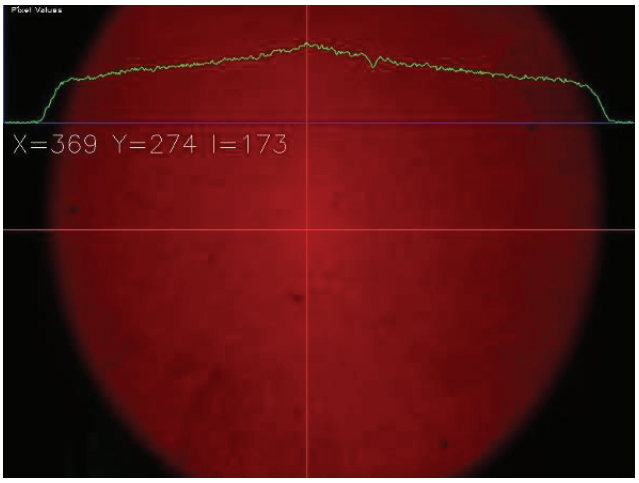

Figure 4. Typical backscattering pattern observed on a camera.

In this way, we have a system capable of observing both large and small scattering cones.

3. Experimental realization

The experimental configuration is schematically presented in figure 3. A helium–neon laser (10 mW at 633 nm) was used as the light source in a polarization preserving configuration. The laser beam was expanded, and its polarization changed to circular, before entering the non-polarizing beam splitter. Scattered radiation was collected by placing an additional objective that projected a real image of the scatterer into zoom objective (Canon EF-S 17–85 mm 1:4-5.6 IS USM) of a CCD camera (Canon EOS 50D). All ghost reflections from optical components were blocked and we were able to observe a clear backscattering pattern. The sample was mounted on a motorized rotation stage, which was used to slightly move the sample during exposure in order to average the speckle.

It was necessary to correct the detected intensities for Fresnel losses inside the optical system preceding the CCD chip. This was done by replacing the scattering sample with a mirror. Its angular position was controlled by a motorized rotation stage. Thus, we were able to record correspondence between the angle of incidence and the detected intensity. This was further used to correct the backscattering measurement results.

We observed and measured the backscattering cones (both wide and narrow) of a range of samples: milk, skin, Teflon, barium sulfate, artificial photonic structures, butterfly and moth wings, etc. A typical backscattering pattern is shown in figure 4.

4. Conclusions

We have described, constructed and tested a zoom system for backscattered radiation detection. It was used to observe both wide and narrow backscattering cones of various biological and artificial samples. The system is easy to construct and use, under the condition that ghost reflections are eliminated.

Acknowledgments

We express our gratitude to the Serbian Ministry of Education and Science for supporting this work through grant numbers III45016 and ON171038.

References

[1] Wiersma D S, van Albada M P and Lagendijk A 1995 *Rev. Sci. Instrum.* **66** 5473–6
[2] Gross P, Störzer M, Fiebig S, Clausen M, Maret G and Aegerter C M 2007 *Rev. Sci. Instrum.* **78** 033105
[3] Kim Y L, Liu Y, Wali R K, Roy H K and Backman V 2005 *Appl. Opt.* **44** 366–77

Defect-guided Airy beams in optically induced waveguide arrays

N. M. Lučić,[1,2] B. M. Bokić,[2] D. Ž. Grujić,[2] D. V. Pantelić,[2] B. M. Jelenković,[2] A. Piper,[2] D. M. Jović,[2] and D. V. Timotijević[2]
[1]*Faculty of Electrical Engineering, University of Belgrade, 73 Bulevar kralja Aleksandra, 11120 Belgrade, Serbia*
[2]*Institute of Physics, University of Belgrade, P.O. Box 68, 11001 Belgrade, Serbia*
(Received 31 October 2013; published 6 December 2013)

We demonstrate both theoretically and experimentally that a finite Airy beam changes its trajectory and shape in optically induced waveguide arrays consisting of different kinds of defects. The propagation dynamics and beam acceleration are controlled with positive and negative defects, and appropriate refractive index change. An additional class of discrete beams and Airy defect modes are demonstrated.

DOI: 10.1103/PhysRevA.88.063815 PACS number(s): 42.25.Bs, 42.65.Jx, 42.82.Et

I. INTRODUCTION

Self-accelerating Airy beams were first demonstrated in quantum mechanics [1] as a dispersion-free solution of the Schrödinger equation. By means of an important link between quantum mechanics and paraxial wave optics, Airy beams have been recently transferred into an optical field [2,3]. They remain invariant along parabolic trajectories and attract a great deal of interest because of their unique properties, including transverse acceleration [4,5], nondiffraction [6,7], and self-reconstruction [8,9]. Such features make these beams useful for applications ranging from guiding and manipulation of microparticles [5] and producing curved plasma channels [10] to dynamically routing surface plasmon polaritons [11,12] and frequency generation [13].

One reason for interest in these beams is their potential application in nonlinear optics regimes: nonlinear interaction of light with some material and a study of accelerating beam dynamics inside nonlinear media. The behavior of Airy beams propagating from a nonlinear medium to a linear medium was studied in Ref. [14]. Formation of self-trapped accelerating optical beams is demonstrated with different self-focusing nonlinearities [15], ranging from Kerr and saturable to quadratic [16,17], and also with an optically induced refractive-index gradient [18]. Recent experimental realization of electron Airy beams [19] opens a novel ways of manipulating Airy beams with various magnetic or electric potentials. Although nondiffracting beams are not stationary solutions of the Schrödinger equation with introduction of uniform waveguide arrays, their modified counterparts are shown to exist and remain nondiffracting [20]. Similarly asymptotic preservation of a free accelerating property is observed [21] with Airy beam introduced in uniform waveguide arrays. This gave us motivation to study the impact of defects in waveguide arrays on uniform waveguide array counterparts of Airy beams.

In this paper, we investigate and analyze both theoretically and experimentally the active control of self-accelerating Airy beams with an optically induced waveguide array consisting of different kinds of defects. Various laser-written waveguide arrays are produced in Fe:$LiNbO_3$ crystal, with periodic refractive index change and appropriate defect guides. We consider how the positive and negative defects [22] influence the beam self-bending as well as reduction of the beam acceleration. In general, we find that with a modification of the refractive index change, Airy beam acceleration can be reduced to the discrete beams. However, close to the defect guides, the beam dynamics changes completely: the beams experience a strong repulsion from the negative defect, while in the presence of the positive defect they form simple localized waves.

II. EXPERIMENTAL REALIZATION AND THEORETICAL MODELING OF AIRY BEAM PROPAGATION IN WAVEGUIDE ARRAYS

We use an iron-doped (0.05%) Fe:$LiNbO_3$ crystal with $0.5 \times 3 \times 10$ mm^3 dimensions. Waveguides are fabricated using the laser-writing system at a laser wavelength of 473 nm, which induces an appropriate structure change in the material [see the schematic diagram in Fig. 1(a)]. By moving the sample with respect to the perpendicular laser beam, a continuous modification of the refractive index is obtained enabling light guiding. The beam is focused by the 50× microscope objective with a numerical aperture (NA) of 0.55. Our sample has waveguides of approximately 10 μm width, with spacing between the centers of the adjacent waveguides of $d = 20\,\mu$m. We fabricate various one-dimensional waveguiding systems with a refractive index change of $\Delta n \sim 1 \times 10^{-4}$, while two of the guides are fabricated with either a lower (negative defect) or higher refractive index change (positive defect), achieved by a variation of the writing velocity. Experimental setup for the investigation of Airy beam propagation in such waveguide arrays is shown in Fig. 1(b). For the creation of the Airy beam, an initial Gaussian beam from a 532 nm laser is projected through a cubic phase mask onto a spatial light modulator (SLM). The beam is then Fourier transformed and the 8 μW input Airy beam, roughly 10 μm wide in the main lobe, is launched to the front face of the crystal. The output intensity pattern, appearing at the end face of the crystal, is real time observed by means of a charge-coupled-device (CCD) camera. The intensity pattern evolution along the propagation direction (z axis) through the crystal is obtained with another CCD camera mounted above the sample, parallel to the x-z crystal plane. The camera records scattered light from the crystal, with the integration time of about 2 min.

To theoretically model Airy beam propagation in a waveguide array, along the propagation distance z, we consider the nonlinear Schrödinger equation

$$i\frac{\partial E}{\partial z} = -\frac{1}{2}\frac{\partial^2 E}{\partial x^2} - V(x)E, \tag{1}$$

where E is a slowly varying envelope, $V(x) = n_s - \Delta n \cos^2(\pi x/d)$ is the periodic refractive-index profile of the

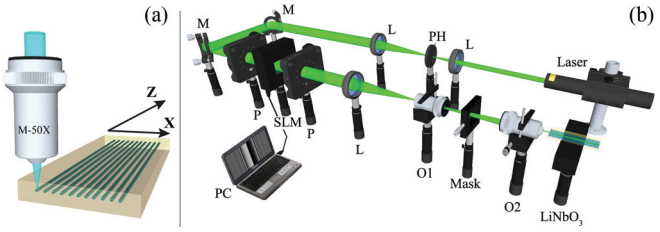

FIG. 1. (Color online) Experimental setup for an investigation of Airy beam propagation effects in waveguide arrays. (a) Scheme of the laser-writing waveguide arrays process in $LiNbO_3$ crystal. (b) Schematic of the experimental setup. Light from a 532 nm laser is expanded and phase modulated by a spatial light modulator (SLM). The beam is Fourier transformed and input into an $LiNbO_3$ crystal, and imaged into a CCD camera. L-lens, PH- pinhole, M-mirror, O-objective, PC-computer.

array with the lattice period d, n_s is a bulk material refractive index, and Δn is the optically induced refractive index change.

We investigate the propagation dynamics of Airy beams in optically induced waveguide arrays, with emphasis on the competition between the acceleration and self-bending propagation properties of Airy beams, and the trend of waveguide arrays to form discrete wave filaments. The propagation characteristics of Airy beams in waveguide arrays with and without defects are considered both theoretically and experimentally. We compare our experimental results to numerical simulations, carried out by the split-step Fourier method with the parameters of our experiment. All theoretical results are confirmed experimentally. First, to compare appropriate effects we test the Airy beam propagation in our crystal with no waveguide arrays fabricated. There is a typical Airy beam bending with a transverse displacement at the output, with no diffraction evident in the main lobe, observed both experimentally [Figs. 2(a) and 2(b)] and theoretically Fig. 2(c), after 10 mm of propagation.

Next, keeping all conditions unchanged, the Airy beam is launched in the waveguide arrays fabricated in our crystal, with the main lobe positioned in one waveguide (an incident waveguide). When refractive index change is optically induced, the Airy beam, which remains self-similar during propagation and has a ballistic trajectory, can interact with the neighboring waveguides. One can see that the bending of the main lobe of the Airy beam is weaker [Figs. 2(d)–2(f)], in comparison with the uniform case [Figs. 2(a)–2(c)]. Also, the presence of the waveguide arrays leads to a creating beam that propagates similar to the discrete waves. With appropriate refractive index change the output position of the Airy beam moves downward, indicating suppressed acceleration of the Airy beam, and it forms the various kinds of discrete structures. A series of numerical investigations are also performed to manipulate Airy beam acceleration with different refractive index change (see Sec. IV, Figs. 4 and 5).

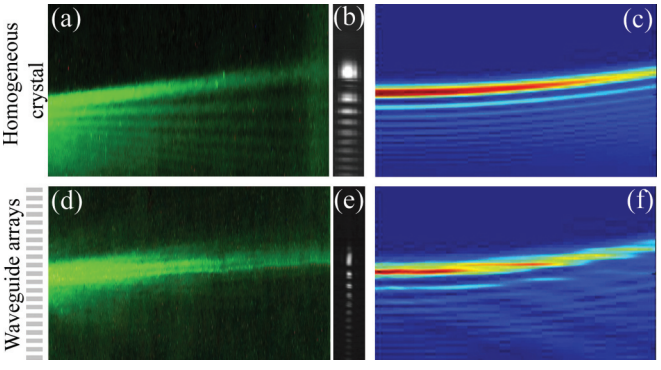

FIG. 2. (Color online) Airy beam propagation in homogeneous $LiNbO_3$ crystal (top row) and waveguide arrays optically induced in the same crystal (bottom row). Intensity plots of Airy beam structures in longitudinal direction during the propagation: (a), (d) experiment; (c), (f) theory. (b), (e) Corresponding intensity distributions at the back face of the crystal. Physical parameters: the crystal length $L =$ 10 mm, lattice constant $d = 20$ μm, width of the main Airy lobe 10 μm.

III. DEFECT-CONTROLLED AIRY BEAM ACCELERATION

We also study the influence of various defect guides on the Airy beam propagation, and active control and manipulation of the beam acceleration with such defects. We show that the balance between self-acceleration properties and defect plays an important role in the evolution of the Airy beam. Our results are shown in Fig. 3, obtained with the same Airy beam as before, but using two different classes of waveguide arrays: containing a single defect with a lower refractive index defect guide (negative defect) and with a higher refractive index defect guide (positive defect). In both cases the main Airy lobe is positioned into the defect guides, at the input. First, we consider waveguide arrays with negative defects and observe strong beam repulsion from such defects [Figs. 3(a)–3(c)]. But, shifting the main lobe position to the waveguide close to the defect channel, one can observe a typical discrete surface waves (not shown). However, the Airy beam propagation is drastically changed in the presence of a positive defect guide so the formation of simple localized waves is possible with appropriate positive defects [Figs. 3(d)–3(f)].

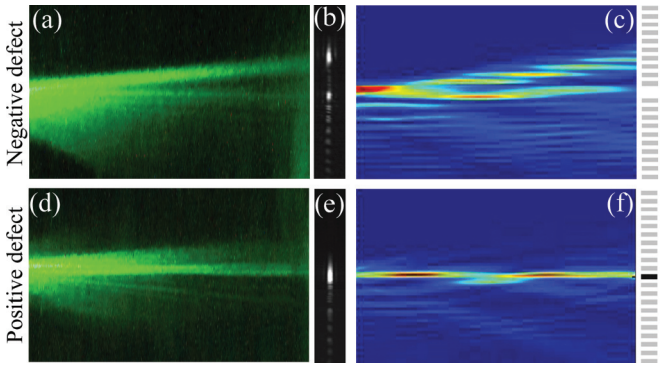

FIG. 3. (Color online) Airy beam propagation in waveguide arrays with negative (top row) and positive (bottom row) defects. Intensity plots of Airy beam structures in longitudinal direction during the propagation: (a), (d) experiment; (c), (f) theory. (b), (e) Corresponding intensity distributions at the back face of the crystal. Defect refractive index change is 0 for negative and $2\Delta n$ for positive defect. Other parameters are as in Fig. 1.

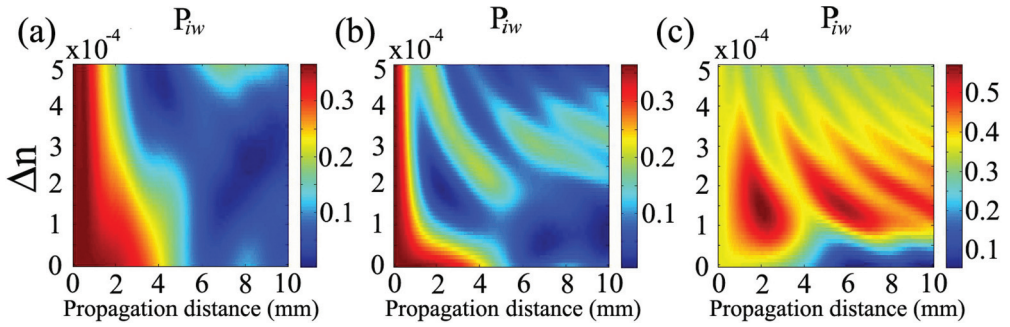

FIG. 4. (Color online) Dependence of the percentage of the Airy beam power in the incident waveguide ($P_{\rm iw}$) on refractive index change Δn and propagation distance for (a) waveguide array, (b) negative defect, and (c) positive defect. Physical parameters are as in Fig. 3.

IV. DEPENDENCE OF AIRY BEAM PROPAGATION ON THE REFRACTIVE INDEX CHANGE

Finally, we study numerically the dynamics of Airy beam propagation in waveguide arrays with various refractive index changes Δn. Again, we compare three cases with positive and negative defects and with no defects. We show that beams exhibit shape-preserving acceleration inside a low refractive index change, but discrete diffraction and formation of various discrete beams occur with an increasing refractive index change, and very rich beam dynamics and amplitude modulations are seen with further increasing of Δn. We monitor a percentage of the Airy beam power in incident waveguide ($P_{\rm iw}$), as the ratio between the power of the beam in the incident waveguide (or defect channel in the case with defect waveguides) and the total power of the Airy beam, at appropriate propagation distance. A dependence of $P_{\rm iw}$ on the refractive index change Δn and propagation distance is presented in Fig. 4 for all three cases: (a) waveguide array, (b) negative defect, and (c) positive defect. Figure 4 clearly demonstrates the impact of waveguide arrays on the formation of discrete beams [Fig. 4(a)]. Also, it demonstrates the impact of the defect inclusion on the acceleration beams, the shape-preserving nature of these beams, and the refractive index change caused with the defect inclusion [Figs. 4(b) and 4(c)]. One can see that discrete beam diffraction is more visible in the case of waveguide arrays without defects. However, an energy localization in the incident waveguide is more pronounced in the waveguide arrays with the negative defect [Fig. 4(b)], and the most with the positive defect [Fig. 4(c)].

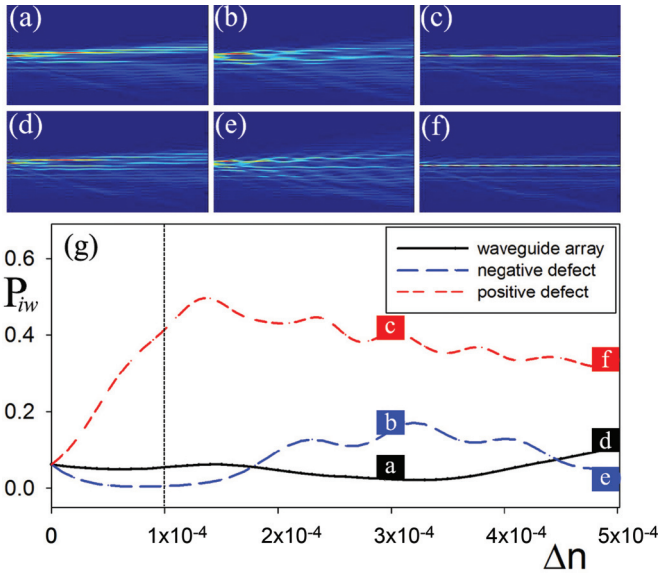

FIG. 5. (Color online) Airy beam propagation dynamics in different waveguide arrays. Typical intensity distributions of Airy beam structures in longitudinal direction during the propagation for waveguide arrays with (a), (d) no defects; (b), (e) negative defect; and (c), (f) positive defect. (a)–(c) $\Delta n = 3 \times 10^{-4}$; (d)–(f) $\Delta n = 5 \times 10^{-4}$. (g) Airy beam power in incident waveguide ($P_{\rm iw}$) at the crystal exit as a function of refractive index change Δn. A vertical dotted line shows experimental refractive index change. Physical parameters are as in Fig. 4.

Figure 5 presents some typical examples of the Airy beam propagation along the longitudinal direction for Δn higher than in our experimental sample. Intensity distributions for two values of refractive index change are shown: $\Delta n = 3 \times 10^{-4}$ (first row) and $\Delta n = 5 \times 10^{-4}$ (second row) for waveguide arrays [Figs. 5(a) and 5(d)], negative defects [Figs. 5(b) and 5(e)], and positive defects [Figs. 5(c) and 5(f)]. In the case without defects, discrete beam formation starts at shorter propagation distance while the refractive index change is increased. With the negative defect guide, increasing Δn, amplitude modulations take place, and they are more pronounced with higher Δn. The beam repulsion from defect guide is also visible. At last, inclusion of a positive defect leads to a more localized energy in the defect guide, but also with some kind of amplitude modulations for higher refractive index change. We monitor Airy beam power in the incident waveguide ($P_{\rm iw}$) at the crystal exit as a function of refractive index change Δn [Fig. 5(g)]. For waveguide arrays with no defects, $P_{\rm iw}$ after 10 mm propagation distance is slightly changed, decreases with lower, but increases with higher Δn. In the case of a negative defect, $P_{\rm iw}$ has maximal values at $\Delta n \sim 3 \times 10^{-4}$. The percentage of the Airy beam power in incident waveguide is higher for positive defect guides, and for parameters we used in our investigation it has maximum at $\Delta n \sim 1.3 \times 10^{-4}$. Also, we investigate defect guides with different refractive index change, as well as different defect size (not shown). Our analysis provides a very good tool for manipulation and controlling of Airy beam acceleration and self -ending properties, as well as appropriate conditions for the formation of discrete, surface or localized waves produced using Airy beams.

V. CONCLUSIONS

In summary, we have demonstrated the propagation dynamics of Airy beams in optically induced waveguide arrays. We have analyzed experimentally and numerically how various waveguides modify acceleration and self-bending properties of such beams, resulting in the discrete beams or Airy defect mode formation. We have demonstrated that the presence of various defect types, their sizes, as well as the refractive index change could drastically change the initial Airy beam shape. The experimental results fully agree with the theoretical analysis. A similar method can be used for control of other accelerating beams, such as parabolic beams. While we performed all our analysis in one-dimensional waveguide arrays, all our findings should also hold in two-dimensional photonic lattices.

ACKNOWLEDGMENTS

This work is supported by the Ministry of Education, Science and Technological development, Republic of Serbia (Projects OI 171036, OI 171038, III 45016).

[1] M. Berry and N. Balazs, Am. J. Phys. **47**, 264 (1979).
[2] G. A. Siviloglou and D. N. Christodoulides, Opt. Lett. **32**, 979 (2007).
[3] G. A. Siviloglou, J. Broky, A. Dogariu, and D. N. Christodoulides, Phys. Rev. Lett. **99**, 213901 (2007).
[4] G. A. Siviloglou, J. Broky, A. Dogariu, and D. N. Christodoulides, Opt. Lett. **33**, 207 (2008).
[5] J. Baumgartl, M. Mazilu, and K. Dholakia, Nat. Photon. **2**, 675 (2008).
[6] I. M. Besieris and A. M. Shaarawi, Opt. Lett. **32**, 2447 (2007).
[7] A. V. Novitsky and D. V. Novitsky, Opt. Lett. **34**, 3430 (2009).
[8] J. Broky, G. A. Siviloglou, A. Dogariu, and D. N. Christodoulides, Opt. Express **16**, 12880 (2008).
[9] H. I. Sztul and R. R. Alfano, Opt. Express **16**, 9411 (2008).
[10] P. Polynkin, M. Kolesik, J. V. Moloney, G. A. Siviloglou, and D. N. Christodoulides, Science **324**, 229 (2009).
[11] P. Zhang, S. Wang, Y. Liu, X. Yin, C. Lu, Z. Chen, and X. Zhang, Opt. Lett. **36**, 3191 (2011).
[12] A. Minovich, A. E. Klein, N. Janunts, T. Pertsch, D. N. Neshev, and Y. S. Kivshar, Phys. Rev. Lett. **107**, 116802 (2011).
[13] T. Ellenbogen, N. Voloch-Bloch, A. Ganany-Padowicz, and A. Arie, Nat. Photon. **3**, 395 (2009).
[14] Y. Hu, S. Huang, P. Zhang, C. Lou, J. Xu, and Z. Chen, Opt. Lett. **35**, 3952 (2010).
[15] I. Kaminer, M. Segev, and D. N. Christodoulides, Phys. Rev. Lett. **106**, 213903 (2011).
[16] A. Lotti, D. Faccio, A. Couairon, D. G. Papazoglou, P. Panagiotopoulos, D. Abdollahpour, and S. Tzortzakis, Phys. Rev. A **84**, 021807(R) (2011).
[17] I. Dolev, I. Kaminer, A. Shapira, M. Segev, and A. Arie, Phys. Rev. Lett. **108**, 113903 (2012).
[18] Z. Ye, S. Liu, C. Lou, P. Zhang, Y. Hu, D. Song, J. Zhao, and Z. Chen, Opt. Lett. **36**, 3230 (2011).
[19] N. Voloch-Bloch, Y. Lereah, Y. Lilach, A. Gover, and A. Arie, Nature **494**, 331 (2013).
[20] O. Manela, M. Segev, and D. N. Christodoulides, Opt. Lett. **30**, 2611 (2005).
[21] R. El-Ganainy, K. G. Makris, M. A. Miri, D. N. Christodoulides, and Z. Chen, Phys. Rev. A **84**, 023842 (2011).
[22] F. Fedele, J. Yang, and Z. Chen, Opt. Lett. **30**, 1506 (2005).

IOP Publishing Physica Scripta
Phys. Scr. **T149** (2012) 014021 (3pp) doi:10.1088/0031-8949/2012/T149/014021

High-resolution dot-matrix hologram generation

Boban Zarkov, Dušan Grujić and Dejan Pantelić

Institute of Physics, Belgrade, Serbia

E-mail: zarkov@ipb.ac.rs

Received 5 September 2011
Accepted for publication 14 November 2011
Published 27 April 2012
Online at stacks.iop.org/PhysScr/T149/014021

Abstract
Holography is a technique that enables us to permanently record three-dimensional (3D) colour pictures. Owing to their sub-micron structure, holograms are remarkable safety devices that are very difficult to counterfeit. Dot-matrix technology, which is one of the commonly used methods, is a substantial obstacle to all types of fraudulent activities. This kind of hologram is mainly used for the purpose of protection against forgery of cheques, cards, passports, etc. Such a high-resolution technique also enables the engineering of 2D and 3D structures, potentially leading to the construction of metamaterials. In this paper, we describe high-resolution holographic structures obtained by dot-matrix devices of novel construction.

PACS numbers: 42.40.Ht, 42.40.Eq

(Some figures may appear in colour only in the online journal)

1. Introduction

A dot-matrix hologram is composed of a large number of micron-sized diffraction grating dots [1]. The fringe period and orientation of each diffraction grating can be controlled by a computer. These diffraction dots are recorded onto a photosensitive material capable of forming a surface relief. The resulting hologram (the so-called master) is used as a first step in the process of mass production (with the embossing technique). Today, the anti-counterfeiting industry uses this technology and provides very high-resolution systems of up to 24 000 dpi.

Because of its high efficiency, large visual angle and kinetic visual effects, dot-matrix holograms are widely used in printing, packing and decoration. They provide a higher degree of security than conventional holograms and can be easily combined with conventional holograms. In this paper, we present the experiential results of our research.

We have developed a device for the generation of dot-matrix holograms with colour images. This system (shown in figure 1) comprises mechanical, electrical and optical components. The whole process is controlled via software, written in Microsoft Visual Studio C++, Express edition. The source of coherent light is a diode pumped solid state (DPSS) laser at a wavelength of 473 nm and an output power of 50 mW.

A motorized *XY* table was used for positioning the photosensitive material with a step resolution of up to 25 nm and a position repeatability of 2 μm. The interference pattern of laser beams was formed on the photosensitive material placed at the focus of a microscope objective (50×0.55 NA). Diffraction gratings obtained this way were 15 μm in diameter and 1 μm in periodicity. The hologram was recorded dot by dot using software for hologram calculation.

2. Generation of dot-matrix holograms

As shown in figure 2, a dot-matrix hologram is composed of small diffraction grating dots [2]. Each dot is a grating whose period and orientation can be modified (under computer control). Grating dots are formed by two-beam interference on the photosensitive material (producing a sinusoidal profile grating pattern). The standard two-beam writing system includes translation and rotation stages to control the period and orientation of grating dots [3]. The photosensitive plate is placed in the focal plane of a microscope objective and the plate is recorded dot by dot. A relief pattern of dot gratings is obtained after proper exposure and chemical development. The final hologram is illuminated with a light beam. The resultant visual effect depends on the diffraction behaviours of all the dots. A well-designed dot-matrix hologram will give

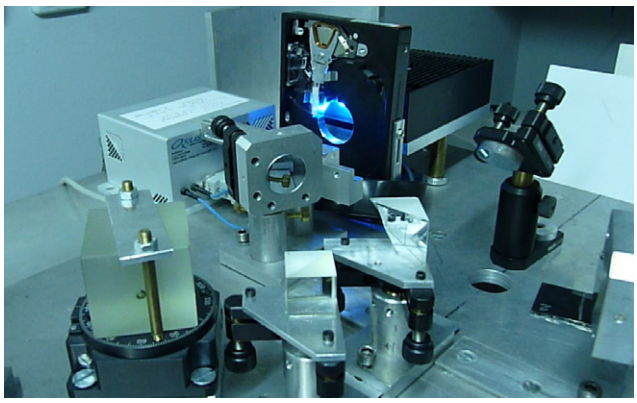

Figure 1. Apparatus for the generation of dot-matrix holograms.

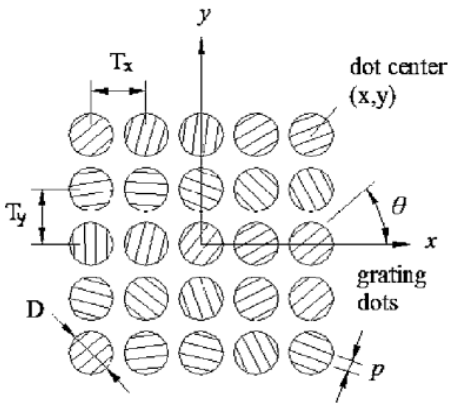

Figure 2. Grating dots on a dot-matrix hologram with five variable parameters: the coordinates T_x and T_y, the grating pitch p, the grating orientation θ and the dot size D.

a wonderful visual effect. It is coloured with dynamical effects due to the change of observation direction.

3. Experimental setup

Figure 3 is a schematic diagram of the system developed for the fabrication of dot-matrix holograms. The device consists of a laser and a beam splitter used to generate two light beams of equal intensity. Beams are directed through the plane parallel plate (mounted on a rotation stage) in order to change their mutual distance. In this way, we were able to control the diffraction grating period. Two beams pass through the dove prism (mounted on another rotation stage), which is used to change the diffraction grating orientation. Finally, beams are focused by a microscope objective onto the photosensitive material mounted on a computer-controlled *XY* table.

Holograms are recorded on a Shipley 1813 photoresist plate mounted on the *XY* translation stage. The substrate was a 20 mm × 20 mm glass slide with a thickness of 1 mm. The photoresist layer coated on the slide was about 2 μm thick. The exposure time for every grating dot was 500 ms. After exposure, the plate was developed in a Shipley 303 developer. The developing time was 15 s. The software (developed in Microsoft Visual Studio) reads an image file and sends the control data to the programmable controllers which coordinate the translation stage, two rotation stages and the shutter. The hologram was recorded dot by dot using a program which determines the parameters for the hologram from the image file. Diffraction gratings obtained this way are shown in figure 4.

All dot-matrix holograms can be designed to create interesting kinetic effects that are brighter and have a broader

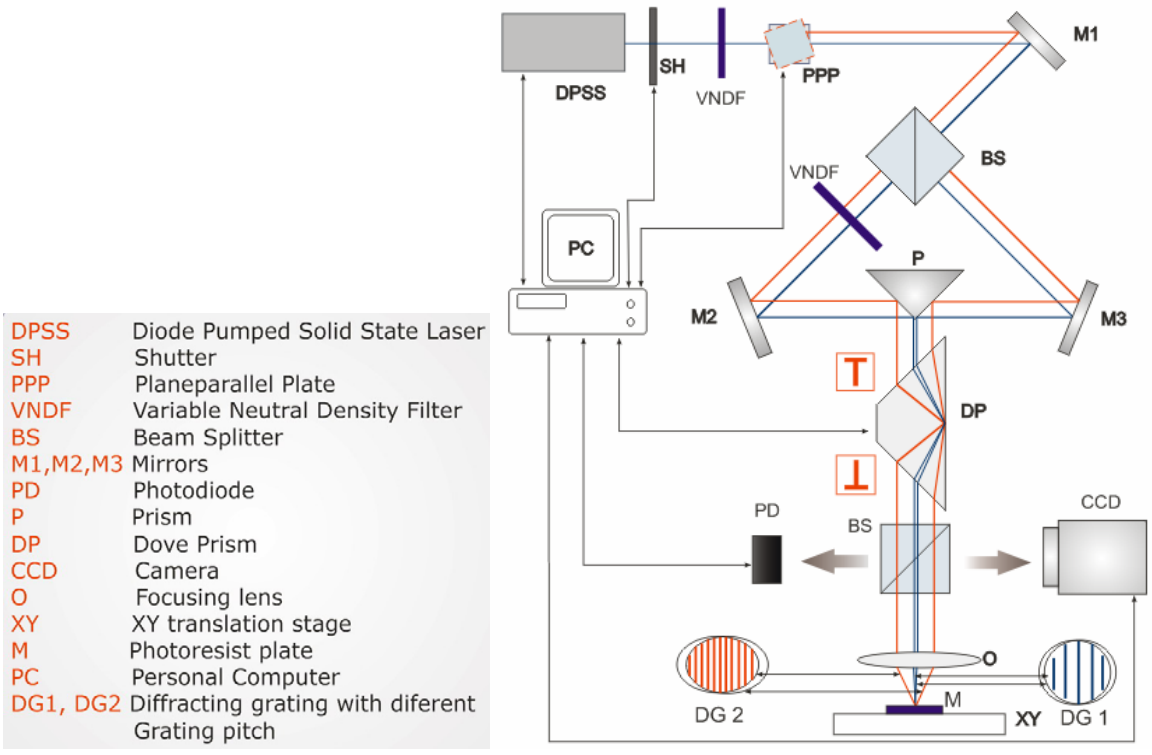

Figure 3. The device setup used for the fabrication of dot-matrix holograms.

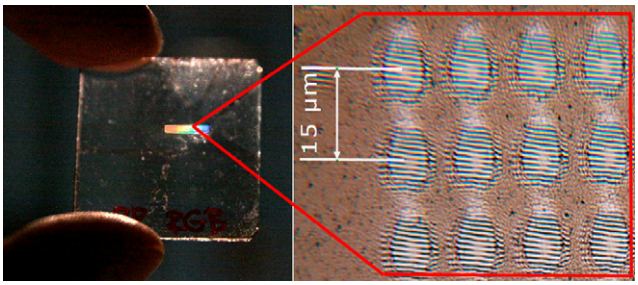

Figure 4. Recorded grating dots on the hologram.

viewing angle when compared with other types of holograms. Higher resolution is needed for microtext and other security features. On the other hand, larger images increase the costs as a result of an increase in the number of pixels that have to be generated.

4. Conclusion

In this work, we have presented a device for the fabrication of computer-generated holograms using the dot-matrix technique. This device consists of mechanical, electrical and optical components that are driven via control and customized recording software. As the source of coherent light emission, we used a DPSS laser with a wavelength of 473 nm and an output power of 50 mW. A motorized *XY* table was used for positioning the photosensitive material. By using mirrors and prisms, we separated two parallel laser beams to the desired distance and introduced them into the microscope objective. We places different photosensitive materials such as pullulan and photoresist in the objective focus in order to obtain the interference patterns of coupled laser beams. Each 15 μm diameter elliptical dot recorded in this way corresponds to a microscopic diffraction grating with 1 μm periodicity.

With such a sophisticated device we have obtained high-resolution safety holograms and we will be able to generate novel metamaterial structures.

Acknowledgment

This work was supported in part by the Ministry of Science and Technology of Serbia under grant no. 45016.

References

[1] Li Y, Wang T, Yang S, Zhang S, Fan S and Wen H 1998 Theoretical and experimental study of dot matrix hologram *Proc. SPIE* **3559** 121
[2] Yeh S L 2006 Dot-matrix hologram with an encrypted figure *Opt. Eng.* **45** 095801
[3] Lee C K *et al* 2000 Optical configuration and color-representation range of a variable-pitch dot matrix holographic printer *Appl. Opt.* **39** 40–53

Praktične primene digitalne holografije

Dejan Pantelić, Dušan Grujić, Darko Vasiljević

Institut za fiziku, Pregrevica 118, 11080 Zemun, Beograd, Srbija

Kontakt: D. Pantelić (pantelic@ipb.ac.rs)

Apstrakt. Sa razvojem kompjutera i tehnologije digitalne registracije slike holografija je i sama zakoračila u digitalnu eru. Umesto klasičnog filma, počeo je da se koristi CCD (ili CMOS) čip kao holografski fotoregistrujući materijal, a analogni proces rekonstrukcije holograma je zamenjen digitalnom obradom. Na taj način je proces registracije i rekonstrukcije holograma postao jednostavniji (jer ne postoji hemijska obrada holograma) i fleksibilniji (jer je hologram sada podložan različitim digitalnim tehnikama obrade slike). Zbog visoke foto-osetljivosti CCD čipa, i mehanički zahtevi su značajno redukovani te je holograme moguće snimati i bez posebnih antivibracionih tehnika.

Ovde će biti prikazani eksperimentalni rezultati primene digitalne holografske interferometrije za merenje malih deformacija i pomeraja. Eksperimentalni uredjaj je specifičan u tom smislu što se predmet nalazi smešten ispred sfernog ogledala, koje stvara realan lik zadnje strane objekta. Koristi se samo jedan laserski snop, koji istovremeno, sa obe strane, osvetljava predmet, a preostali deo snopa biva fokusiran ogledalom i služi kao referentni snop. Time se omogućava istovremeno posmatranje objekta i sa prednje i sa zadnje strane, što daje kompletnu informaciju o ispitivanom predmetu. Holografska slika se registruje na standardnoj SLR kameri Canon EOS 50d, koja ima visoku rezoluciju od 4752 x 3168 piksela. Obrada registrovanog holograma se vrši primenom Frenelovog transforma na računaru sa nVidia (CUDA enabled) karticom, čime je omogućeno paralelno procesiranje. Kao rezultat, vreme obrade holograma veličine 2048 x 2048 piksela je oko 5 sekundi.

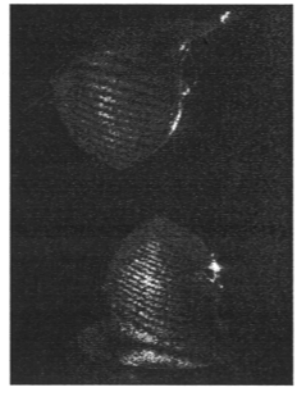

Slika 1. Digitalni hologram deformacije zuba izazvane polimerizacionom kontrakcijom.

U uredjaju smo ispitivali mehaničke deformacije zubnog tkiva izazvane polimerizacijom zubne ispune. Proces polimerizacije je praćen kontrakcijom koja se prenosi na zubno tkivo. Holografska interferometrija nam je omogućila da odredimo maksimalnu defomaciju zubnog tkiva. Uredjaj je korišćen i za ispitivanje mehaničkih procesa u zubu tokom dejstva spoljašnjih sila (mastikacija). Stereolitografijom je formiran model zuba koji je zatim mogao da bude opterećen u realnom, holografskom, eksperimentu, ali i da se opterećenja proračunavaju metodom konačnih elemenata. Dobijeni interferogrami omogućavaju proračun mehaničkih opterećenja, kao i dinamičko praćenje čitavog procesa.

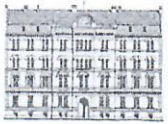

Република Србија
Универзитет у Београду
Физички факултет
Д.Бр.2011/8015
Датум: 18.12.2015. године

На основу члана 161 Закона о општем управном поступку и службене евиденције издаје се

УВЕРЕЊЕ

Грујић (Живојин) Душан, бр. индекса 2011/8015, рођен 24.02.1984. године, Крушевац, Крушевац-град, Република Србија, уписан школске 2015/2016. године, у статусу: самофинансирање; тип студија: докторске академске студије; студијски програм: Физика.

Према Статуту факултета студије трају (број година): три.
Рок за завршетак студија: у двоструком трајању студија.

Ово се уверење може употребити за регулисање војне обавезе, издавање визе, права на дечији додатак, породичне пензије, инвалидског додатка, добијања здравствене књижице, легитимације за повлашћену вожњу и стипендије.

Овлашћено лице факултета

FIZIČKI FAKULTET
UNIVERZITETA U BEOGRADU
Broj 2972010
Beograd, 18. 10. 2010. godine

Na osnovu člana 161. Zakona o opštem upravnom postupku i člana 4. Pravilnika o sadržaju i obliku obrazaca javnih isprava koje izdaju više škole, fakulteti i univerziteti, po zahtevu, Grujić Duana izdaje se sledeće

U V E R E N J E

GRUJIĆ (ŽIVOJIN) DUŠAN, rodjen 24. 02. 1984. godine u Kruševcu, R. Srbija upisana školske 2003/2004. godine na studijsku grupu **FIZIKA** smer **Primenjena fizika i informatika** položio je ispite predvidjene nastavnim planom i programom navedene Studijske grupe i diplomirao na Fizičkom fakultetu Univerziteta u Beogradu 13. oktobra 2010. godine, sa srednjom ocenom 8,14 (osam i 14/100) u toku studija i ocenom 10 (deset i 00/100) na diplomskom ispitu i time stekao visoku stručnu spremu (VII_1 stepen stručne spreme) i stručni naziv

DIPLOMIRANI FIZIČAR ZA PRIMENJENU FIZIKU I INFORMATIKU

Uverenje se izdaje na lični zahtev, a služi kao dokaz o završenoj visokoj stručnoj spremi (VII_1 stepen stručne spreme) do izdavanja diplome.

Uverenje je oslobodjeno plaćanja takse.

D E K A N
FIZIČKOG FAKULTETA

Prof. dr Ljubiša Zeković

Преглед научне активности

У току 2011. и 2012. године Душан Грујић је био ангажован као истраживач на реализацији уређаја за формирање тзв. дот-матрикс холограма. Због специфичности начина уписивања оваквих холограма на фоторегиструјући материјал потребна је координација свих елемената на уређају, то јест усаглашен рад механичких и оптичких елемената, те је доста рађено на унапређењу комуникације софтвера са опремом која служи за позиционирање одговарајуће оптике, као и самог материјала на коме се врши уписивање дијаграма. Касније је ова апаратура надограђена тако да се на њој могу ласерским снопом генерисати оптички индуковане фотонске структуре у нелинеарном медијуму. Као нелинеарни медијум је коришћен литијум-ниобат допиран гвожђем, у облику танког правоугаоног блока (апроксимација једнодимензионе структуре). Струтуре су реализоване у виду низа таласовода који су уписивани интензивним ласерским зрачењем нормалним на површину блока, при чему се исти помера аутоматским дводимензионим позиционером. Ова мултифункционална апаратура може служити и за фабрикацију миркосочива, биомиметичких структура, а у плану је надоградња исте тако да може служити и као дигитални холографски миркоскоп.

Научна активност Душана Грујића је примарно базирана на експериментима који се тичу дигиталне холографије и њене примене на мерење структура и деформација малих димензија. За потребе ових експеримената је учествовао у развијању холографске методе снимања објеката у више димензија. То подразумева израду специфичне експерименталне поставке којом се обезбеђује квалитетније прикупљање информација о сниманом објекту , као и израду софтвера којим се врши снимање и нумеричка реконструкција дигиталног холограма Френеловом трансформацијом где је за убрзавање целокупног процеса обраде уведено коришћење NVIDIA графичких картица и CUDA протокола паралелног процесирања. Холограм се региструје директно на CCD чип камере која је повезана са рачунаром на ком се складиште подаци и веома брзо извршава обрада захваљујући паралелном процесирању. На овај начин је остварена уштеда у времену и материјалу у односу на аналогни начин обраде који се користио раније. Такође, могуће је један исти холограм реконструисати више пута (што код аналогне није могуће), са различитим нумеричким параметрима у циљу добијања што боље реконструкције. Коришћењем метода холографске интерферометрије могу се добити информације о деформацији, снимањем и упоређивањем два холограма истог објекта у различитим условима. Обзиром да се у поставци експеримента користи сферно огледало, слика која се добија је у већини случајева закривљена. Знајући параметре огледала и користећи могућност пропагације уназад, део кода за аутоматску корекцију слике је успешно имплементиран.

Колега Грујић се бави и генерисањем различитих врста тзв. недифрагујућих зрака, што подразумева оптимизацију рада одговарајућих ласера, припремом зрака за пролазак кроз просторни модулатор светлости, генерисање одговарајуће фазне слике на модулатору и просторно филтрирање по проласку зрака кроз модулатор. Идеја је да се због великог губитка снаге ласерског снопа услед проласка кроз просторни модулатор светлости, направи холограм траженог зрака, те да се он касније користи у експерименту, замењујући просторни модулатор светлости.